Article

Cell Reports

Dissonant Representations of Visual Space in Prefrontal Cortex during Eye Movements

Graphical Abstract

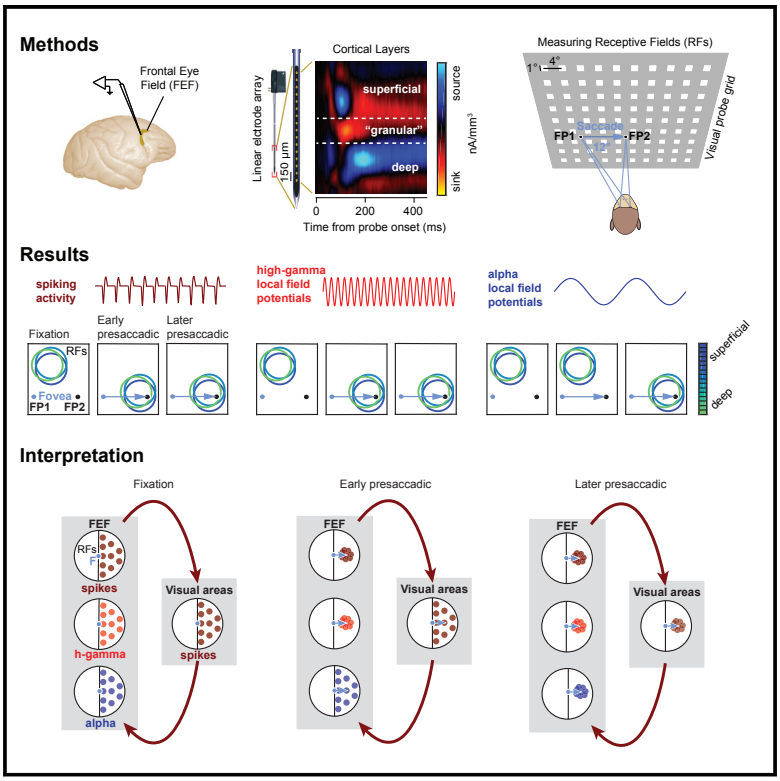

Highlights

- Spatial information is high in low and high LFP frequencies in prefrontal cortex
- Spatial visual signals in LFPs and spikes are robust across cortical layers
- Across fixations, LFP and spiking receptive fields (RFs) are retinocentric
- During saccades, high-gamma and spiking RFs converge, followed by alpha RFs

Authors

Xiaomo Chen, Marc Zirnsak, Tirin Moore

Correspondence

xiaomo@stanford.edu

In Brief

Chen et al. report dissonant representations of visual space in prefrontal cortex, carried in the spiking activity and the local field potentials (LFPs), which ultimately converge toward the goal of saccadic eye movements. These observations have important implications for the neural mechanisms underlying visual perception during eye movements.

Chen et al., 2018, Cell Reports *22*, 2039–2052
February 20, 2018
https://doi.org/10.1016/j.celrep.2018.01.078

CellPress

Cell Reports
Article

Dissonant Representations of Visual Space in Prefrontal Cortex during Eye Movements

Xiaomo Chen,[1,2,3,4,*] Marc Zirnsak,[1,2,3] and Tirin Moore[1,2]
[1]Department of Neurobiology, Stanford University School of Medicine, Stanford, CA 94305, USA
[2]Howard Hughes Medical Institute, USA
[3]These authors contributed equally
[4]Lead Contact
*Correspondence: xiaomo@stanford.edu
https://doi.org/10.1016/j.celrep.2018.01.078

SUMMARY

We used local field potentials (LFPs) and spikes to investigate representations of visual space in prefrontal cortex and the dynamics of those representations during eye movements. Spatial information contained in LFPs of the frontal eye field (FEF) was differentially distributed across frequencies, with a majority of that information being carried in alpha and high-gamma bands and minimal signal in the low-gamma band. During fixation, spatial information from alpha and high-gamma bands and spiking activity was robust across cortical layers. Receptive fields (RFs) derived from alpha and high-gamma bands were retinocentrically organized, and they were spatially correlated both with each other and with spiking RFs. However, alpha and high-gamma RFs probed before eye movements were dissociated. Whereas high-gamma and spiking RFs immediately converged toward the movement goal, alpha RFs remained largely unchanged during the initial probe response, but they converged later. These observations reveal possible mechanisms of dynamic spatial representations that underlie visual perception during eye movements.

INTRODUCTION

Local field potentials (LFPs) are low-frequency extracellular voltage fluctuations that reflect multiple sources (Buzsáki et al., 2012; Einevoll et al., 2013), including synaptic activity (Haider et al., 2016; Mitzdorf, 1985), action potentials (Berens et al., 2011; Ray and Maunsell, 2011), and intrinsic voltage-dependent membrane responses (Silva et al., 1991). The study of LFPs thus provides a unique window into synaptic processes and neural networks at multiple temporal and frequency scales. In the primate brain, LFPs have been extensively studied and linked to visual stimulus coding (Henrie and Shapley, 2005; Katzner et al., 2009; Liu and Newsome, 2006; Ray and Maunsell, 2010), visual attention (Buschman and Miller, 2009; Fries et al., 2001; Gregoriou et al., 2014), and perceptual reports (Gail et al., 2004; Wilke et al., 2006; Wimmer et al., 2016; Womelsdorf et al., 2006), and they have been demonstrated to provide additional information over the spiking activity about the underlying neural mechanisms. For example, recent evidence suggests that, in cortex, lower LFP frequencies (6–16 Hz, which include the alpha band) reflect synaptic inputs from distal subcortical and cortical sources (Belitski et al., 2008; Saalmann et al., 2012; van Kerkoerle et al., 2014; Vijayan and Kopell, 2012), whereas higher frequencies (80–150 Hz, high-gamma band) reflect processes from more local sources (Ray et al., 2008; Ray and Maunsell, 2010). LFPs can thus provide information about the underlying neural circuitry of visual processing.

The neural representation of visual space relies on the receptive field (RF) organization of neurons throughout the visual system. A number of studies have demonstrated that the RFs of visual neurons can change due to behavioral demands (Connor et al., 1996; Merrikhi et al., 2017; Moran and Desimone, 1985; Reynolds et al., 1999; Tolias et al., 2001). In particular, neuronal responses tend to be enhanced for stimuli that are covertly attended (Fries et al., 2001; Kastner and Ungerleider, 2001; Luck et al., 1997; Reynolds and Chelazzi, 2004) or are the targets of saccadic eye movements (Chelazzi et al., 1993; Desimone et al., 1994; Fischer and Boch, 1981; Moore et al., 1998; Moore and Zirnsak, 2017; Sheinberg and Logothetis, 2001). In the latter case, RF changes appear to emerge shortly before movement onset. Saccades provide a severe challenge to the visual system as they lead to substantial displacements of the retinal image. Paradoxically, although perception is stable across saccades, strong perceptual distortions occur during these movements when probed experimentally, and these distortions are thought to provide clues about the mechanisms underlying the illusion of stability (Burr et al., 2010). Recently, we reported that the RFs of neurons within prefrontal cortex (frontal eye field [FEF]) converge toward the location of eye movement targets prior to the movement (Zirnsak and Moore, 2014; Zirnsak et al., 2014). This convergence provides a neuronal correlate of the overriding perception of target space during saccades (Zhao et al., 2012), and it suggests a basis for the illusion of stability during such movements (Deubel et al., 1996).

The FEF is heavily interconnected with most extrastriate areas within posterior visual cortex, and thus the origin of its RF dynamics remains an important question. To address this question, we analyzed the LFPs in the FEF, together with the spiking activity, both during fixation and during saccadic eye movements. LFPs provide a means to investigate the interaction of local

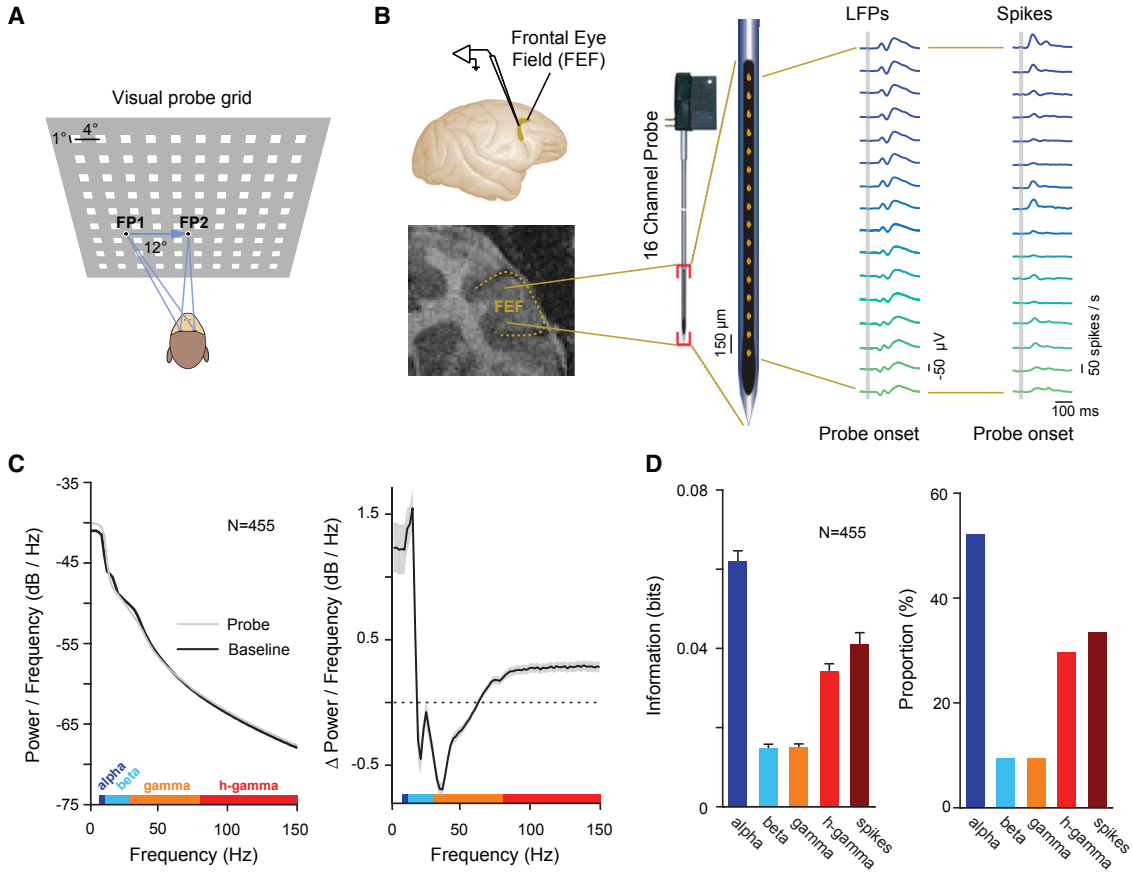

Figure 1. Measuring Visual Spatial Representation across LFP Frequency Bands and Spiking Activity during Fixation and Saccadic Eye Movements

(A) A probe stimulus (white square) was briefly presented while monkeys maintained stable fixation (at FP1 or FP2) or while they prepared an eye movement from FP1 to FP2.

(B) FEF neural responses were recorded with 16-channel linear arrays. Top left shows location of the FEF in the macaque brain. Bottom left shows coronal magnetic resonance image of the FEF in monkey N.

(C) The left graph shows the LFP power spectra for baseline (black) and visual responses (gray). The right graph shows the difference between the two power spectra. The gray shaded area denotes the SEM. LFP frequency bands (alpha, beta, low gamma, and high gamma) used for analyses are shown color coded on top of the x axis.

(D) The left graph shows the average *MI* about probe location contained within the LFP responses for a given frequency band (Figure S1) and contained within the spikes, both as measured during fixation. Error bars denote the SEM. The right graph shows the percentage of electrode sites across all experimental sessions yielding statistically significant *MI* for the different LFP bands and spikes.

neuronal networks with other networks in distal subcortical and cortical areas, which provide synaptic input to this network (Einevoll et al., 2013) and, thus, can illuminate the origin of RF dynamics in the FEF. We first asked how much visual spatial information can be derived from different frequency bands of FEF LFPs across cortical layers. Next, we asked whether the RFs derived from LFPs were retinocentrically organized and whether they correlated with those derived from the spiking activity. Finally, we examined the dynamics of LFP-derived RFs during eye movements.

RESULTS

We measured LFP and spiking responses to brief (25-ms) visual probe stimuli during fixation at a first fixation point (FP1; fixation 1), during fixation at a second fixation point (FP2; fixation 2), as well as shortly before saccadic eye movements from FP1 to FP2 (presaccadic) (Figure 1A). The location of probe stimuli (90) was pseudorandomly varied across a 36 × 32-degree of visual angle (dva) part of visual space. We recorded LFPs and spiking activity within the FEFs of two monkeys (*Macaca mulatta*) with 16-channel laminar electrodes (U-Probes, Plexon) (Figure 1B). In total, LFPs and multi-unit spiking activity were recorded from 455 FEF sites (Experimental Procedures).

Visual Spatial Information in FEF LFPs Is Differentially Distributed across Frequency Bands

We first analyzed visual responses in the LFPs by comparing the power spectrum before and after the presentation of probes during fixation (Figure 1C). Our analysis of LFPs focused on four

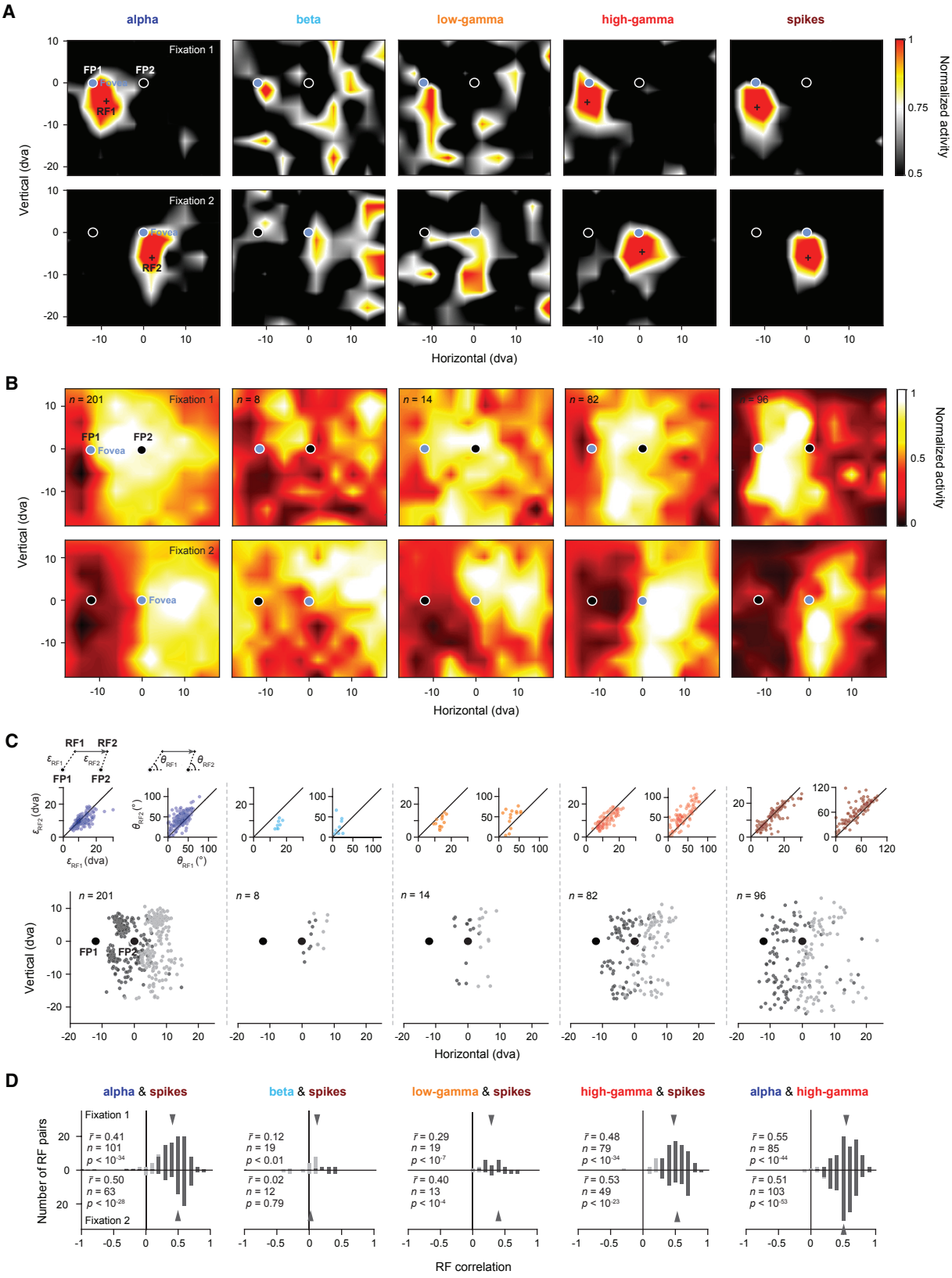

(legend on next page)

candidate frequency bands known to contain visual information (Einevoll et al., 2013; Tremblay et al., 2015), specifically the low-frequency bands, centered on alpha (8–12 Hz), the beta band (12–30 Hz), the low-gamma band (30–80 Hz), and the high-gamma band (80–150 Hz). Results were qualitatively identical when using frequency bands defined on the basis of signal correlations (Experimental Procedures). In contrast to previous studies in posterior visual areas, where enhanced power (*P*) in response to visual stimulation was observed in beta and low-gamma bands (Burns et al., 2010; Liu and Newsome, 2006), we observed increased power in the alpha ($\overline{\Delta P}$ = 1.237 dB, $p < 10^{-5}$) and high-gamma bands ($\overline{\Delta P}$ = 0.253 dB, $p < 10^{-5}$) and suppressed power in the beta ($\overline{\Delta P}$ = −0.553 dB, $p < 10^{-5}$) and low-gamma bands ($\overline{\Delta P}$ = −0.164 dB, $p < 10^{-4}$).

We next measured the visual spatial information contained in the probe-driven responses within the selected frequency bands. To do this, we computed the mutual information (*MI*) between the responses and the probe locations (Experimental Procedures). Consistent with the observed enhancement of alpha and high-gamma power in the visual response, we found that most of the spatial information was contained within those bands ($\overline{MI}_{alpha}$ = 0.062 bits; $\overline{MI}_{high\ gamma}$ = 0.034 bits; ANOVA, $p < 10^{-88}$) (Figure 1D, left). Furthermore, the proportion of recording sites with significant *MI* was greatest in the alpha (52.20%) and high-gamma (29.74%) bands (Figure 1D, right). Thus, alpha and high-gamma bands showed the strongest positive visual responses and contained most of the information about probe location.

Alpha and High-Gamma RFs Are Retinocentrically Organized during Fixation and Spatially Correlated with Spiking Activity and Each Other

We next tested whether visual RFs could be derived from the different LFP frequency bands. Figure 2A shows an example recording in which the *MI* analysis revealed significant spatial information in the alpha and high-gamma bands (MI_{alpha} = 0.093 bits, $p < 0.001$; $MI_{high\ gamma}$ = 0.055 bits, $p < 0.001$), but not the beta and low-gamma bands (MI_{beta} = 0.007 bits, p = 0.717; $MI_{low\ gamma}$ = 0.000 bits, p = 0.681). Consistent with that observation, clear RFs could be derived from the former two bands, but not the latter. Across the two fixation locations, the LFP-derived RFs exhibited a retinocentric pattern; that is, the RFs and their centers were largely independent of the orbital position of the eye, and they were displaced in an amount approximately equal to the displacement of the fovea between fixations (Figure 2A, first and fourth columns), similar to the RFs derived from the spiking activity (Figure 2A, fifth column).

To examine the retinocentricity of RFs across the population of recordings and within each LFP band, we analyzed all recordings with significant visual spatial information (Experimental Procedures) during both fixation 1 and fixation 2. Figure 2B shows the population RFs (Experimental Procedures) for all significant recordings of each LFP band. Similar to the spiking population RFs, those in the alpha and high-gamma bands were displaced across the two fixations in a manner roughly equal to the change in fixation. In contrast, the displacement pattern across the two fixations was less clear for the beta- and low-gamma-derived population RFs. A similar pattern of results was obtained when we only examined the centers of each RF (Figure 2C). To quantify this result, we computed the correlation between the eccentricity (ε) and direction (θ) of each RF during fixation 1 and fixation 2 (Experimental Procedures). Similar to the eccentricities and directions of RFs derived from the spiking activity, eccentricities, and directions of RFs derived from alpha and high-gamma activity were significantly correlated across fixations (alpha: r_{ε} = 0.67, $p < 10^{-26}$, r_{θ} = 0.66, $p < 10^{-25}$; high gamma: r_{ε} = 0.80, $p < 10^{-18}$, r_{θ} = 0.81, $p < 10^{-19}$; spikes: r_{ε} = 0.86, $p < 10^{-28}$, r_{θ} = 0.80, $p < 10^{-21}$). However, there were no significant correlations observed for beta- and low-gamma-band RFs (beta: r_{ε} = 0.70, p = 0.06, r_{θ} = 0.07, p = 0.87; low gamma: r_{ε} = 0.48, p = 0.08, r_{θ} = 0.44, p = 0.12), presumably because there were too few significant RFs in those bands to begin with.

In the example recording (Figure 2A), alpha- and high-gamma-band RFs were significantly correlated with the RF derived from the spiking activity (fixation 1: $r_{alpha,\ spikes}$ = 0.25, $p < 0.01$; $r_{high\ gamma,\ spikes}$ = 0.63, $p < 0.001$; fixation 2: $r_{alpha,\ spikes}$ = 0.32, $p < 0.001$; $r_{high\ gamma,\ spikes}$ = 0.48, $p < 0.001$). This pattern of results was also observed across the population of recordings. RFs derived from the alpha and high-gamma bands were significantly correlated with the spiking-derived RFs in 89.90% (90/101) and 96.20% (76/79) of all significant recordings during fixation 1 and 92.06% (58/63) and 95.92% (47/49) during fixation 2, respectively (fixation 1: $\bar{r}_{alpha,\ spikes}$ = 0.41, $p < 10^{-34}$; $\bar{r}_{high\ gamma,\ spikes}$ = 0.48, $p < 10^{-34}$; fixation 2: $\bar{r}_{alpha,\ spikes}$ = 0.50, $p < 10^{-28}$; $\bar{r}_{high\ gamma,\ spikes}$ = 0.53, $p < 10^{-23}$) (Figure 2D). Across the two fixations, the correlation between spiking RFs and high-gamma RFs was slightly greater than between spiking RFs and

Figure 2. Retinocentricity of LFP- and Spiking-Derived RFs

(A) Five example response maps derived from different LFP frequency bands (alpha, beta, low gamma, and high gamma) and spikes recorded simultaneously from one recording site. Response maps shown in the top row were measured during stable fixation at FP1 (fixation 1) (Experimental Procedures; Figure 4A). The cross in each map indicates the estimated RF1 center. Response maps shown in the bottom row were measured during fixation at FP2 (fixation 2). The cross in each map indicates the estimated RF2 center. The RFs have been spatially interpolated and smoothed for visualization.

(B) Population RFs based on all significant RFs from individual electrode sites as measured during fixation 1 (top row) and fixation 2 (bottom row). The population RFs have been spatially interpolated and smoothed for visualization.

(C) Populations of RF centers across fixations (RF1s in dark gray and RF2s in light gray). Insets on the top left of each graph show correlations between the distance from RF1 to FP1 (ε_{RF1}) and the distance from RF2 to FP2 (ε_{RF2}) for the respective population of RF centers. Solid lines depict the line of unity. Insets on the top right of each graph show the correlation between the two smallest absolute angles θ_{RF1} and θ_{RF2} formed by the horizontal meridian and ε_{RF1}, respectively ε'_{RF2} (Experimental Procedures). Solid lines depict the line of unity.

(D) Histograms of correlations between LFPs and spikes across frequency bands, based on pairs of significant RFs measured during fixation 1 (top row) and fixation 2 (bottom row). Rightmost histogram shows the correlation between alpha and high gamma. Darker bars indicate statistically significant correlations. Gray arrows indicate the mean of the respective distribution.

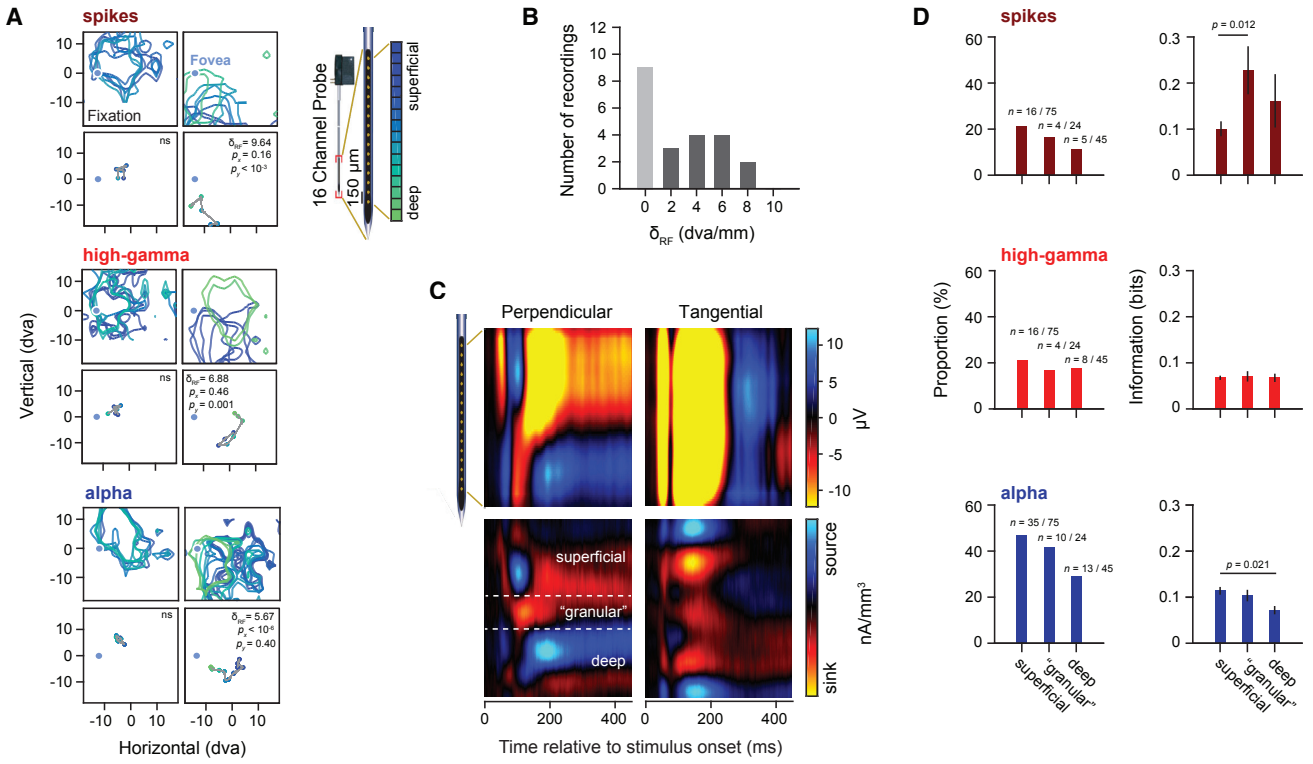

Figure 3. Visual Spatial Information across FEF Layers

(A) Examples of perpendicular (left) and tangential (right) recordings plotted separately for spike, alpha-, and high-gamma-band RFs. RF contours indicate plus 1 SD after Z-transformation of the individual RFs. The bottom row of each panel depicts the corresponding RF centers. RF contours and RF centers are plotted as a function of channel depth. Recordings with significant RF displacements across electrodes (δ_{RF}) were classified as tangential with respect to the cortical layers, whereas recordings with non-significant RF displacements were classified as perpendicular.

(B) Histogram showing the number of perpendicular (light gray) and tangential recordings (dark gray).

(C) LFP responses across all probe locations during fixation and corresponding CSDs for a perpendicular and tangential recording. The CSD map has been spatially smoothed for visualization.

(D) Proportion of significant RFs and amount of *MI* for significant recordings during fixation across cortical compartments. Error bars denote the SEM.

alpha RFs ($\bar{r}_{\text{high gamma, spikes}} - \bar{r}_{\text{alpha, spikes}} = 0.05$, $p = 0.03$). Very few of the recordings showed significant correlations with the spiking RFs in the beta (fixation 1: 7/19; fixation 2: 4/12) and low-gamma bands (fixation 1: 17/19; fixation 2: 11/13).

Consistent with their correlations with the spiking RFs, alpha and high-gamma RFs were also correlated with each other. In the example (Figure 2A), the correlation amounted to $r_{\text{alpha, high gamma}} = 0.62$ ($p < 0.001$) for fixation 1 and to $r_{\text{alpha, high gamma}} = 0.40$ ($p < 0.001$) for fixation 2. Across the population of recordings, 95.2% (81/85) showed significant correlations during fixation 1 ($\bar{r}_{\text{alpha, high gamma}} = 0.55$, $p < 10^{-44}$) and 96.1% (99/103) showed significant correlations during fixation 2 ($\bar{r}_{\text{alpha, high gamma}} = 0.51$, $p < 10^{-53}$) (Figure 2D, right).

RFs and Spatial Information from Alpha- and High-Gamma-Band and Spiking Activities Were Robust across Cortical Layers

Next, we asked whether LFP-derived RFs and spatial information are differently distributed across FEF cortical layers. Since the majority of the FEF is buried within the arcuate sulcus, it is more difficult to position microelectrodes perpendicular to the cortical surface than it is in other cortical areas that lie largely on the surface (Buffalo et al., 2011; Chandrasekaran et al., 2017; Godlove et al., 2014; Nandy et al., 2017). However, at least some portions of the FEF extend onto the gyral surface (Bruce et al., 1985; Gerbella et al., 2010; Huerta et al., 1987; Schall et al., 1995), where perpendicular electrode penetrations are possible. Indeed, we found that some of our linear array recordings were obtained from largely perpendicular penetrations based on the lack of visual RF displacement across electrode array channels, as observed in previous studies within visual cortex (Engel et al., 2016; Nandy et al., 2017) (Figure 3A). We observed clear examples of recordings with little or no RF displacement of LFP or spike-derived RFs, as well as recordings in which the RFs were significantly displaced across channels (Figure 3A). We found that 9 of the 29 recordings were made perpendicular to the cortical surface (Figure 3B) (Experimental Procedures). For these putative perpendicular recordings, we then used current source density (CSD) analysis (Mitzdorf, 1985; Nicholson and Freeman, 1975) to identify superficial layers, an input (granular) layer (Bruce et al., 1985), and deeper layers of the FEF (Figure 3C) (Experimental Procedures), similar

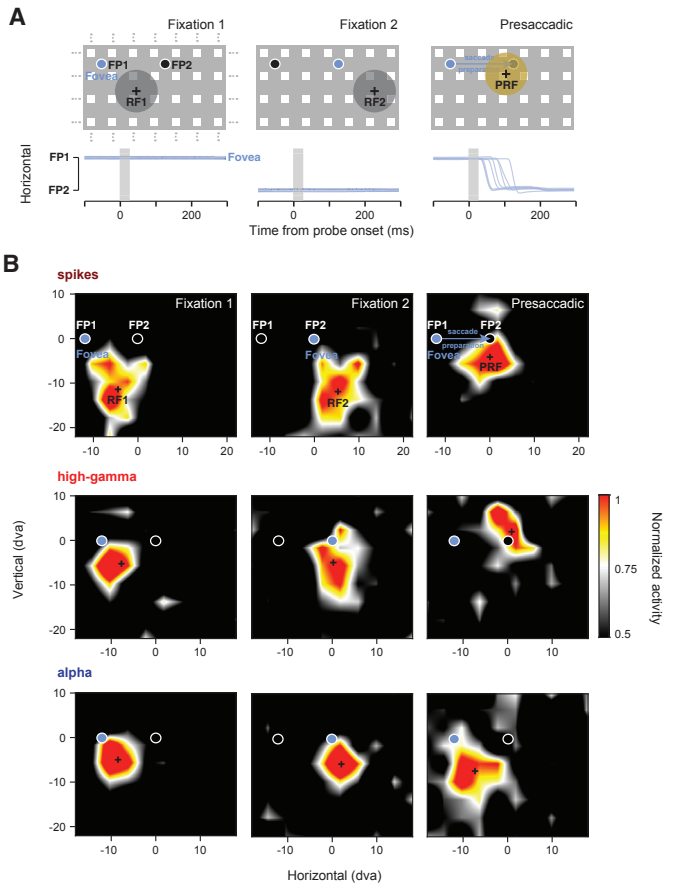

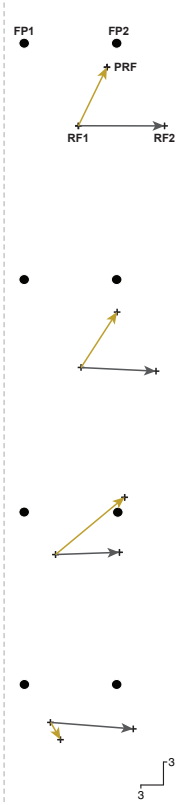

Figure 4. Changes in RFs at the Time of Saccadic Eye Movements

(A) Illustration of previous observations on presaccadic RF changes of FEF neurons (Zirnsak et al., 2014). Following an eye movement from fixation point 1 (FP1) to fixation point 2 (FP2), FEF RFs (gray disks) remain fixed in retinocentric coordinates when measured during fixation (fixation 1 and fixation 2). When measured during saccade preparation to FP2, while the animal is still fixating at FP1, FEF RFs (gold disk) shift toward the eye movement target. Blue traces indicate horizontal eye position from one animal over time for a number of example trials. The gray shaded area indicates the timing and duration of the probe. Crosses in each panel indicate the respective fixation RF centers (RF1 and RF2) and the presaccadic RF center (PRF). The vectors on the right show the displacement of the RF center across fixations (gray) and the presaccadic shift toward the saccadic target (gold).

(B) The top row shows an example spiking RF as measured during the three experimental periods (fixation 1, fixation 2, and presaccadic). Crosses in each panel indicate the RF centers as used in the vector plots. The middle row shows an example high-gamma RF and the bottom row shows an example alpha. RFs have been spatially interpolated and smoothed for visualization.

to studies in other cortical structures (Godlove et al., 2014; Nandy et al., 2017; Schroeder et al., 1998).

Using data obtained solely from perpendicular penetrations, we analyzed the amount of visual spatial information contained within the three identified cortical compartments during fixation for the alpha, high-gamma, and spiking activities (Figure 3D). Although there was a trend toward fewer significant RFs in deeper layers, particularly for the spiking and alpha activities, there was no significant difference in the proportions of RFs across layers (Fisher's exact test, $p_{spikes} = 0.46$, $p_{high\ gamma} = 0.88$, and $p_{alpha} = 0.16$). However, for recordings yielding significant RFs, we observed a significant difference in *MI* across cortical layers for the spiking and alpha activities (ANOVA, $p_{spikes} = 0.02$ and $p_{alpha} = 0.02$) (Figure 3D, right column). *Post hoc* pairwise comparisons revealed a significant difference between superficial and granular layers for the spiking-derived RFs, with higher *MI* contained within the granular layers ($p = 0.012$, t-test with Bonferroni correction). For the alpha-band-derived RFs, we observed greater *MI* contained within the superficial layers as compared to deep layers ($p = 0.021$, t-test with Bonferroni correction).

Dissociation of Alpha and High-Gamma RFs during Eye Movements

We previously reported that RFs based on the spiking activity of FEF neurons converge toward the saccadic target prior to movement onset (Zirnsak et al., 2014). We therefore tested whether the RFs derived from alpha and high-gamma bands also converge toward the target during saccade preparation (Experimental Procedures; Figure S2). For these tests, we combined perpendicular and tangential recordings as both yielded the same pattern of results, with no clear trend across cortical layers. First, for comparison, we computed spiking RFs and their centers using responses to probes flashed during fixation 1 (RF1) and fixation 2 (RF2) and during the presaccadic period (PRF) using responses to probes flashed shortly before the movement (Experimental Procedures). Figure 4A illustrates the pattern of results for FEF neurons described previously in which the PRFs shift toward the saccadic target (FP2). The example spiking RF shown in Figure 4B (top row) demonstrates both the retinocentricity of spiking RFs (gray arrow) and the shift of the PRF toward the target (gold arrow). The latter effect differed between RFs derived from alpha and high-gamma bands. In the same time period in which spiking RFs exhibited shifts toward the saccade target ([0, 250] ms from probe onset), we found that high-gamma band RFs showed the same shifts (Figure 4B, middle row). In contrast, during that period, alpha RFs remained largely at the RF1 location (Figure 4B, bottom row). Thus, in the presaccadic period, alpha and high-gamma RFs were spatially dissociated.

The dissociation of alpha and high-gamma RFs was also observed across the population of significant RFs (Figure 5). As expected, PRFs derived from the spiking activity aligned to probe onset ([0, 250] ms) exhibited clear shifts toward the saccadic target (Figure 5A). That is, the PRFs were significantly closer to the target (FP2) than their corresponding RF1s

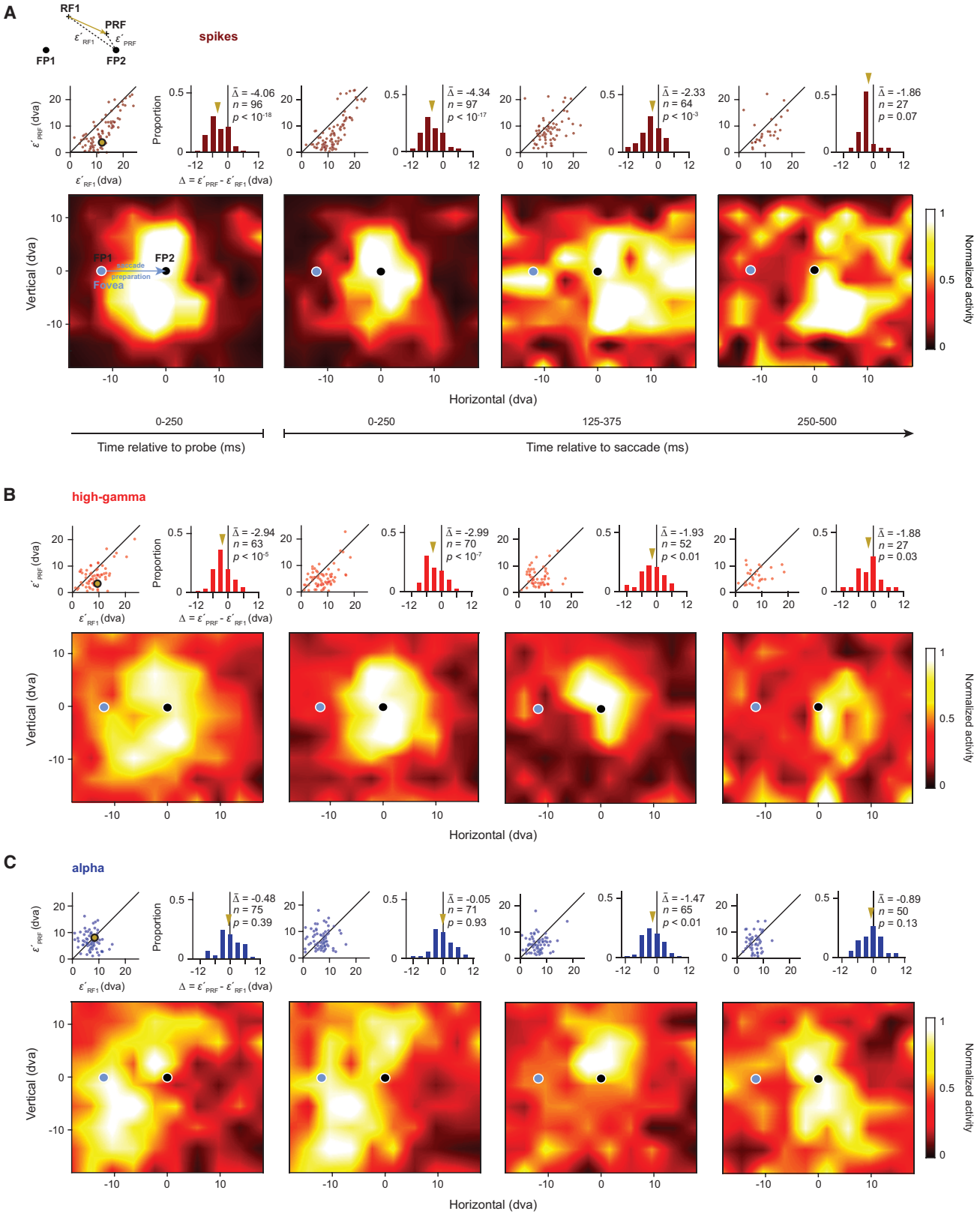

(legend on next page)

($\varepsilon'_{PRF} - \varepsilon'_{RF1} = -4.06$ degrees, $p < 10^{-18}$) (Figure S3 contrasts the PRFs and RF2s). In addition, these shifts were evident in the spiking activity aligned to saccade onset, although the shift did not reach significance in the last time bin, corresponding to the decrease in number of measurable RFs ([0, 250] ms: −4.34 degrees, $p < 10^{-17}$; [125, 375] ms: −2.33 degrees, $p < 10^{-3}$; [250, 500] ms: −1.86 degrees, p = 0.07). Similar to the PRF shifts in the spiking activity, we observed early shifts of PRFs derived from high-gamma LFPs (Figure 5B). In the probe-aligned responses, high-gamma PRFs were significantly closer to the target than their corresponding RF1s ($\varepsilon'_{PRF} - \varepsilon'_{RF1} = -2.94$ degrees, $p < 10^{-5}$). High-gamma PRF shifts were also evident in the responses aligned to saccade onset. Moreover, these shifts were significant across all three saccade-aligned time bins ([0, 250] ms: −2.99 degrees, $p < 10^{-7}$; [125, 375] ms: −1.93 degrees, p = 0.004; [250, 500] ms: −1.88 degrees, p = 0.03). Thus, the high-gamma RFs exhibited clear shifts toward the target when probed during saccade preparation, and they did so in a manner similar to the RFs derived from the spiking activity.

During the initial presaccadic probe response, in contrast to PRFs in the high-gamma band, alpha-band PRFs exhibited no significant shifts (Figure 5C). Instead, the distance between alpha PRFs and the target remained equal to the distance between the RF1 and the target across the population of RFs. There was no evidence of a shift in either the probe-aligned PRFs ($\varepsilon'_{PRF} - \varepsilon'_{RF1} = -0.48$ degree, p = 0.39) or in the initial saccade-aligned PRFs (0.05 degree, p = 0.93). However, by the second, saccade-aligned time bin ([125, 250] ms), the PRF shift toward the target emerged (−1.47 degrees, p < 0.01). This shift was similar in magnitude to the shift evident in the same time bin of the high-gamma PRFs (Figure 5B). In the final time bin, the alpha-band PRF shift was still apparent but no longer significant (−0.89 degree, p = 0.13). Thus, the alpha-band and high-gamma-band PRFs were dissociated from each other during saccade preparation; high-gamma PRFs shifted first toward the target, similar to the spiking PRFs, followed then by alpha PRFs. The sequence of PRF shifts was also evident in a subset of recording sites with significant RFs in both the alpha and high-gamma bands (paired RFs, Figure 6A). In this dataset, the probe-aligned high-gamma PRFs were closer to the saccadic target than their corresponding alpha PRFs ($\varepsilon'_{alpha\ PRF}/\varepsilon'_{alpha\ RF1} - \varepsilon'_{high\text{-}gamma\ PRF}/\varepsilon'_{high\text{-}gamma\ RF1} = 0.302$, p = 0.001). For the saccade-aligned responses, this difference was largest in the earliest time bin ([0, 250] ms: 0.270, $p < 10^{-3}$; [125, 375] ms: 0.151, p = 0.047), but it was no longer significant in the last one ([125, 375] ms: 0.006, p = 0.979). This dissociation between alpha and high-gamma PRFs cannot be explained by a lack or delay of signal in the alpha band, as the probe-evoked activity emerges earlier and is stronger in the alpha band as compared to the high-gamma band (matching pursuit decomposition; Chen et al., 2010; Ray et al., 2008) (Figure S6).

Next, we analyzed the presaccadic shifts separately for perpendicular recordings and tangential recordings, as well as presaccadic shifts across different cortical layers. Consistently, for both set of recordings, as for the complete set of recordings, we found that in the initial presaccadic probe response ([0, 250] ms, saccade aligned), RFs derived from spikes and from the high-gamma band converged immediately toward the saccadic target (perpendicular recordings: spikes −3.65 degrees, p = 0.009; high gamma −3.45 degrees, p = 0.04; tangential recordings: spikes −6.07 degrees, $p = 4.35 \times 10^{-11}$; high gamma −4.58 degrees, $p = 1.52 \times 10^{-4}$), whereas RFs derived from the alpha band did not (perpendicular recordings: 0.58 degree, p = 0.70; tangential recordings: 0.43 degree, p = 0.64). In the subsequent time period ([125,375] ms), however, the alpha RFs converged as well (perpendicular recordings: −2.73 degrees, p = 0.009; tangential recordings: −2.33 degrees, p = 0.03). Thus, we observed the same overall dissociation between the alpha-band RFs and high-gamma-band and spiking-derived RFs in our perpendicular recordings as we did for the complete dataset. Finally, we looked for differences in the magnitude of the RF shifts across cortical layers. Although some trends could be observed, e.g., stronger mean shift in spiking RFs measured within the granular layer, none of the cross-laminar comparisons reached statistical significance (ANOVA, 0–250 ms: spikes p = 0.42, high gamma p = 0.53, alpha p = 0.72; 125–375 ms: spikes p = 0.14, high gamma p = 0.43, alpha p = 0.19). However, it is possible that with a much larger number of significant RFs, differences between laminar compartments might emerge.

As a consequence of the early dissociation between alpha and high-gamma PRFs, we found that, across the entire presaccadic response ([0, 500] ms, saccade aligned), the correlation between the alpha PRFs and the spiking PRFs was significantly less than the correlation between the high-gamma and the spiking PRFs ($\bar{r}_{alpha,\ spikes} - \bar{r}_{high\ gamma,\ spikes} = -0.17$, $p < 10^{-2}$) (Figure 6B; Figure S7A), and there were disproportionately fewer significant correlations between alpha and spiking PRFs than between high-gamma and spiking PRFs (45% versus 83%, chi-square = 4.40, p = 0.04). In addition, we compared the spiking and LFP RF correlations between the fixation (fix) and presaccadic (pre) epochs. For both the alpha and high-gamma RFs, the

Figure 5. Dissociation of Alpha and High-Gamma RFs at the Time of Eye Movements

(A) Spiking population RFs during saccade preparation. Each map shows the population RF based on responses at different times relative to the eye movement (from left to right, population RF aligned to probe onset [0–250] ms, population RFs aligned to saccade onset [0–250] ms, [125–375] ms, and [250–500] ms). The insets on top of each population RF compare the distance ε'_{PRF} between the presaccadic RF centers (PRFs) and the saccade target (FP2) to the distance ε'_{RF1} between the fixation 1 RF centers (RF1s) and the FP2 for all significant presaccadic RFs of a given time (Experimental Procedures; Figure S3). Solid lines in the scatterplots depict the line of unity. The gold dot corresponds to the example RF shown in Figure 3B. Gold arrows in the histograms indicate the mean of the population.

(B) High-gamma population RFs. The same conventions were used as in (A).

(C) Alpha population RFs. The same conventions were used as in (A). All population RFs and RF centers are based on, respectively from, statistically significant individual presaccadic RFs. Figure S4 shows the same results for all presaccadic RFs independent of their statistical significance. Figure S5 shows the PRF versus RF2 comparison for this RF population. Population RFs have been spatially interpolated and smoothed for visualization.

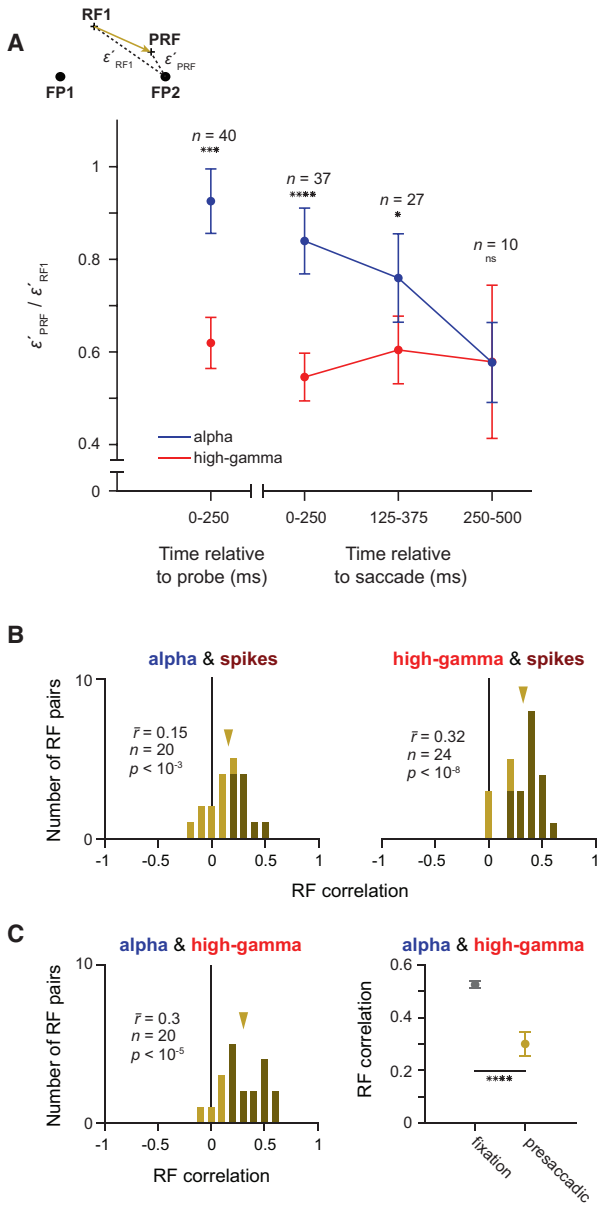

Figure 6. Asynchronous RF Convergence of Alpha and High-Gamma RFs and Correlations with Spiking RFs

(A) Ratio of ε'_{PRF} (distance between the PRF and FP2) to ε'_{RF1} (distance between the RF1 and FP2) for paired alpha (blue) and high-gamma (red) RFs from the same recording site. Ratios are plotted for the same time epochs relative to the eye movement as in Figure 4. Asterisks indicate a significant difference between the alpha and high-gamma band (*$p < 0.05$, ***$p < 10^{-3}$, and ****$p < 10^{-4}$). Error bars denote the SEM.

(B) Correlation histograms based on pairs of significant presaccadic RFs within different LFP bands. Darker bars indicate statistically significant correlations. Gold arrows indicate the mean of the respective distribution.

(C) Correlation between presaccadic alpha and high-gamma RFs (left) was reduced compared to the fixation period (right). Error bars denote the SEM.

correlations were reduced in the presaccadic period. However, there was a significantly larger reduction in RF correlations in the alpha band ($\bar{r}^{fix}_{alpha,\ spikes} - \bar{r}^{pre}_{alpha,\ spikes} = -0.30$, $\bar{r}^{fix}_{high\ gamma,\ spikes} - \bar{r}^{pre}_{high\ gamma,\ spikes} = -0.18$, permutation test, $p = 0.04$). Finally, we sought to determine whether the dissociation of presaccadic RFs could be observed solely between alpha and high-gamma bands. Consistent with previous results, we found that the correlation between alpha PRFs and high-gamma PRFs (Figure 5C, left) was significantly lower during the presaccadic epoch than during fixation (Figure 6C, right) ($\bar{r}^{pre}_{alpha,\ high\ gamma} - \bar{r}^{fix}_{alpha,\ high\ gamma} = -0.17$, $p < 10^{-6}$; see also Figure S7B). Correspondingly, there were fewer recordings showing significant correlations between alpha and high-gamma RFs in the presaccadic epoch (75%) than in the fixation epoch (96%) (chi-square = 13.28, $p < 10^{-3}$).

DISCUSSION

Distribution of Visual Spatial Information across the LFP Spectrum in Prefrontal Cortex

Previous studies have examined visual information contained in stimulus-driven LFPs within primate posterior visual cortex. These studies have generally observed that a majority of information about visual stimuli, such as contrast (Henrie and Shapley, 2005; Ray and Maunsell, 2010), size (Gieselmann and Thiele, 2008), orientation (Frien et al., 2000; Gray and Singer, 1989; Katzner et al., 2009), direction of motion (Liu and Newsome, 2006), the content of natural scenes (Belitski et al., 2008), and, like the present study, stimulus location (Eckhorn et al., 1988; Mineault et al., 2013; Self et al., 2016), is robustly contained within the low-gamma band (30–80 Hz). In contrast, our results within the FEF differ from these studies in that we observed a marked paucity of visual information in the low-gamma band. We observed not only a lack of a clear increase in low-gamma power in response to visual stimulation during fixation but also little to no visual spatial information in the low-gamma band. This result is consistent with a modeling study that predicts relatively low-gamma power in prefrontal cortex (Mejias et al., 2016), and a recent study reporting superior encoding of stimulus position from high-gamma activity within lateral prefrontal cortex (Tremblay et al., 2015). The apparent lack of visual information in the low-gamma band within prefrontal cortex could be due to fundamental differences in cytoarchitecture and connectivity between visual and prefrontal cortex (Barbas and Pandya, 1989; Gabbott and Bacon, 1996). Consistent with this possibility, evidence in rodents indicates that parvalbumin-positive (PV+) interneurons, which are less numerous in frontal cortex (Tremblay et al., 2016; Xu et al., 2010), contribute directly to low-gamma power (Cardin et al., 2009) and the encoding of sensory signals (Siegle et al., 2014). This evidence could account for the relative lack of visual spatial information in the FEF low-gamma band.

Local versus Distal Origin of RF Dissociation

We observed at least two separable dynamics of visual spatial information in the FEF around the time of eye movements, which were contained in the alpha band and in the high-gamma band and spikes. The dissociation of alpha and high-gamma spatial signals suggests possible sources of spiking RF changes within the FEF and the structures with which it connects. Here we

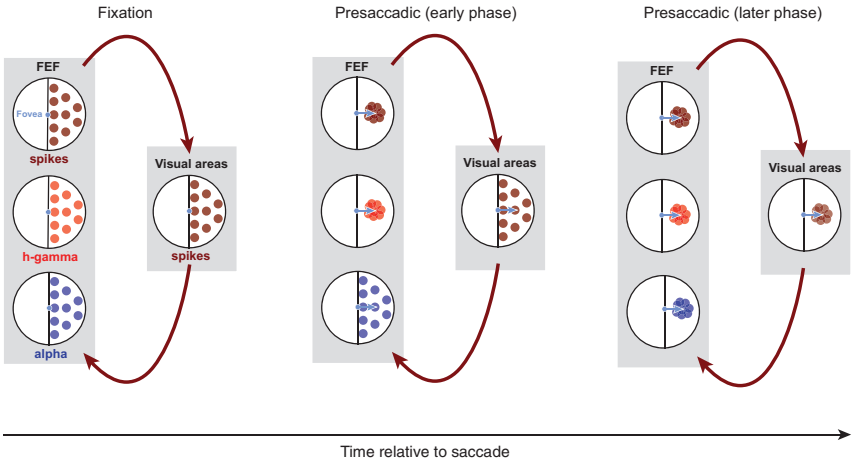

Figure 7. Possible Basis for Separable Dynamics of Spatial Information during Eye Movements

Black circles represent the visual field; colored dots denote RFs. Dark red dots indicate spiking RFs in the recorded visual field. Red dots indicate high-gamma RFs and blue dots indicate alpha RFs. The schematic depicts that high-gamma RFs may be largely generated locally within the FEF, whereas the alpha RFs may largely reflect the synaptic input from upstream structures. Arrows indicate the signal flow between areas. Shortly before a saccade, the convergence of RFs toward the movement goal could originate first from FEF neurons and be associated with a similar convergence in the high-gamma activity. At the same time, synaptic inputs from distal sources, reflected in the alpha band, might largely maintain their retinocentric representation. Subsequently, as a result of recurrence with the FEF, visual inputs to the FEF could gradually begin to exhibit RF convergence as well.

discuss four possible scenarios that may account for our observations, based on the two frequency bands having either rather local or distal origins in this network. In two of these scenarios, alpha signals are largely generated locally within the FEF, whereas high-gamma signals are largely generated either locally or distally. Given the decorrelation of spikes and the alpha band signals during the eye movement, these two scenarios, although possible, seem unlikely. That is, the alpha signals appear more likely to be dominated by inputs from neurons located outside the FEF (Belitski et al., 2008; Saalmann et al., 2012; van Kerkoerle et al., 2014), i.e., inputs that evoke post-synaptic signals at membranes within the FEF.

In a third scenario, both the alpha and high-gamma signals may largely originate from distal sources, and they may reflect synaptic input from cortical and/or subcortical structures connected with the FEF. For example, the two different bands may reflect different input streams (e.g., synaptic inputs from dorsal and ventral visual pathways, which come together within the FEF; Schall et al., 1995; Stanton et al., 1995; Ungerleider and Desimone, 1986). Since it is known that dorsal inputs have shorter visual latencies than ventral inputs (Chen et al., 2007; Schmolesky et al., 1998), in this scenario, the slower alpha RF dynamics could originate from more ventral stream sources, whereas the faster high-gamma dynamics could originate from more dorsal stream sources. Although the nature of RF dynamics during eye movements remains controversial within posterior areas providing synaptic input to the FEF (e.g., lateral intraparietal area [LIP]) (Duhamel et al., 1992; Hamker et al., 2008; Wang et al., 2016; Zirnsak and Moore, 2014), there is evidence of RF convergence in at least area V4 (Hartmann et al., 2017; Tolias et al., 2001), which provides direct input to the FEF. Thus, in this scenario, these ventral inputs would exhibit RF dynamics subsequent to those in dorsal areas. However, as we discuss below, evidence suggests that it is unlikely that high-gamma signals are generated predominantly from distal sources of synaptic inputs. Moreover, there is no evidence yet that different visual input streams are represented in different frequency bands.

In a fourth scenario, high-gamma activity may be largely generated locally within the FEF, whereas the alpha band activity may largely reflect the synaptic input from distal structures, that is, neurons located outside the FEF. This scenario is consistent with evidence that high-gamma band power originates mostly from local sources, for example, through spike synchronization (Ray et al., 2008; Ray and Maunsell, 2011), and lower frequencies from more distal sources, which could include both cortical (Khawaja et al., 2009; van Kerkoerle et al., 2014) and subcortical structures (Belitski et al., 2008; Einevoll et al., 2013; Saalmann et al., 2012; Vijayan and Kopell, 2012). Power in the high-gamma band tends to be correlated with spikes in many cortical regions, including primary visual cortex (Rasch et al., 2008; Ray and Maunsell, 2011), the middle temporal area (Liu and Newsome, 2006), posterior parietal regions (Hwang and Andersen, 2012; Pesaran et al., 2002), and secondary somatosensory cortex (Ray et al., 2008). In contrast, low-frequency activity tends to be uncorrelated with the spiking activity in many respects. For example, in early visual cortex, low-frequency LFP power (<12 Hz) and spiking activity encode independent visual information about naturalistic stimuli (Belitski et al., 2008). In addition, low-frequency LFP power in early visual cortex is more closely related to the perception (Gail et al., 2004; Wilke et al., 2006) than the local spiking activity. If indeed alpha- and high-gamma-band activities in the present study reflect more distal and more local signals, respectively, then the observed RF dynamics contained in the alpha band, the high-gamma band, and the spiking activity could reflect an interaction between the FEF and its connected areas. In this interaction, convergence of RFs toward the movement goal could originate first from FEF neurons and be associated with a similar convergence in the high-gamma-band activity. At the same time, synaptic inputs from distal visual sources, measured in the alpha band, might largely maintain their retinocentric representation. Subsequently, as a result of recurrence with the FEF, synaptic inputs to the FEF could gradually begin to exhibit RF convergence (Figure 7). Although speculative, given the current evidence, we view this scenario as the most likely of the four.

Implications for Visual Perception during Eye Movements

In humans and other primates, visual exploration is achieved through a series of saccadic eye movements; each movement shifting gaze to bring objects of interest to the fovea for further processing. Although these movements lead to frequent and substantial displacements of the retinal image, these displacements are not perceived. It is widely believed that the illusion of this visual stability during eye movements results from an active compensatory mechanism, such as corollary discharge (e.g., Sommer and Wurtz, 2006), which effectively reduces or eliminates the impact of visual disruptions resulting from saccades (Sommer and Wurtz, 2004; Wurtz, 2008). This compensatory mechanism is also thought to be reflected by the profound impairments in visual perception that occur at the time of saccades. For example, the ability of human observers to localize stimuli at the time of saccades is severely impaired. Typically, observers perceive the location of stimuli as being much closer to the saccadic target than their veridical location (Kaiser and Lappe, 2004; Ross et al., 1997). It has been suggested that this distortion of perceptual space can be explained by a distortion of the neuronal population response toward the saccadic target (Hamker et al., 2008). Consistent with that hypothesis, spiking-derived RFs of V4 neurons (Hartmann et al., 2017; Tolias et al., 2001) and FEF neurons (Zirnsak et al., 2014) shift closer to the saccadic target when measured around the time of the movement. Indeed, the convergence of RFs in the FEF correlates with the systematic distortions in perceptual space reported for human observers (Zirnsak et al., 2014; Zirnsak and Moore, 2014). In addition to observing a similar convergence in the LFPs, our observation of dissociated alpha- and high-gamma-band RFs, and the resulting dissonance in their spatial representations, adds perhaps another possible basis for perceptual mislocalization. Shortly before saccade onset, visual space represented in the alpha band differs dramatically from that represented in the high-gamma band, and the emergence of these dissonant visual representations, when combined, may increase the uncertainty in stimulus position contained in the FEF. Indeed, mislocalization in human observers consists both of systematic errors in perceptual judgments and of an apparent decrease in the precision of those judgments (Hamker et al., 2008). Given the FEF's extensive connectivity with posterior visual cortex (Schall et al., 1995), and it's clear role in visual perception (Moore and Zirnsak, 2017), it seems unlikely that such dissonant signals would have no impact on perception. Finally, the fact that both the alpha and the high-gamma representations ultimately converge toward the movement target suggests that an overrepresentation of target space emerges within the FEF and connected visual areas. This overrepresentation reflects the dominant perception of the target, a perception that appears to override the retinal displacements caused by eye movements (Deubel et al., 1996; McConkie and Currie, 1996).

EXPERIMENTAL PROCEDURES

We used two male adult monkeys (*Macaca mulatta*, 12 and 8 kg) in the experiments. All experimental procedures were in compliance with the US Public Health Service policy on the humane care and use of laboratory animals, the Society for Neuroscience Guidelines and Policies, and Stanford University Animal Care and Use Committee. General surgical and standard electrophysiological procedures are described in the Supplemental Experimental Procedures.

RF Measurements

We measured LFP- and spiking activity-derived RFs during stable fixation and shortly before saccades within the FEF by pseudorandomly presenting a single-probe stimulus out of a 10 × 9 probe grid extending 36 × 32 dva. In each recording session, we placed the probe grid to cover the area where we expected most of the RFs based on evoked saccade vectors by microstimulation of a given recording site. Details of the RF measurements are described in the Supplemental Experimental Procedures.

LFP- and Spiking-Derived RFs, Centers, and Their Correlations

To estimate RFs, we first computed probe-response maps (e.g., Figure 2A) as follows: for a given probe location, trial, and time interval, we obtained the mean LFP power by calculating the mean of the power spectral density (PSD) for each frequency band (alpha, 8–12 Hz; beta, 12–30 Hz; low gamma, 30–80 Hz; and high gamma, 80–150 Hz) or, in the case of the spiking activity, the spike count. We chose these frequency bands for easier comparisons to previous studies. However, the results were qualitatively identical when we instead used frequency bands (low frequency, 5–20 Hz; low-medium frequency, 20–40 Hz; medium-high frequency, 40–80 Hz; and high frequency, 80–150 Hz), based on signal correlations between different frequencies (Figure S7).

We then computed the average power or activity for each probe location as the arithmetic mean across all trials. This was done separately for the two fixation and the presaccadic conditions. Only response maps yielding significant *MI* (see below) were considered as significant RFs.

After assessing the statistical significance of a given RF, the RF center (x_c, y_c) in Cartesian coordinates was then computed as the center of mass for all locations passing the following criteria: first, the response of a given location had to be no less than the average response across all locations plus 1 SD; and second, a given location had to be surrounded by at least two directly adjacent probe locations with responses no less than the average response.

We then defined the eccentricity (ε) and the direction (θ) as the distance and angle between a given RF center to the fixation point (x_f, y_f):

$$\varepsilon = \sqrt{(x_f - x_c)^2 + (y_f - y_c)^2}, \quad \text{(Equation 1)}$$

$$\theta = \arccos((x_f - x_c)/\varepsilon). \quad \text{(Equation 2)}$$

Pearson's *r* was then calculated between eccentricity and direction pairs for the RF measurements obtained during fixations 1 and 2 to quantify their retinocentricity. The correlation was calculated individually for all four LFP frequency bands and the spiking activity (Figure 2C).

In addition, 2D signal correlations were computed to quantify the similarity between two given RFs *i* and *j*. The correlation is defined as

$$r = \frac{\sum_x \sum_y (RF_{i,x,y} - \overline{RF_i})(RF_{j,x,y} - \overline{RF_j})}{\sqrt{\left(\sum_x \sum_y (RF_{i,x,y} - \overline{RF_i})^2\right)\left(\sum_x \sum_y (RF_{j,x,y} - \overline{RF_j})^2\right)}}, \quad \text{(Equation 3)}$$

where $RF_{i,x,y}$ and $RF_{j,x,y}$ denote the activity of RF_i and RF_j at probe location (x,y) and $\overline{RF}$ denotes the mean activity across all locations. In addition to quantifying the similarity between LFP RFs and spiking RFs (Figures 2 and 6), this metric was used to quantify the similarity between LFP RFs or spiking RFs with RFs at adjacent recording sites with varying distances during simultaneous recording (Figure S7).

Nonparametric permutation tests (1,000 repetitions) were used to assess the significance of a given correlation. The resulting average correlation obtained from the permutation procedure was subtracted from all reported correlation values.

Finally, population RFs were computed to visualize how the representations of visual space change before saccades. For each condition (fixation 1, fixation 2, and presaccadic), we first averaged individual RFs with adjacent centers. Visual space was divided into equally sized bins (6 × 4 dva) centered around the saccade target (FP2). RFs with centers falling inside the same bin were then simply averaged (arithmetic mean). The average RFs for each bin were then normalized and averaged again to obtain the final population RF. This method optimizes estimations of visual space representations by minimizing effects due to sampling biases of the measured RFs.

MI Analysis

To quantify the spatial information about the probe stimulus *S* contained within LFPs and the spiking activity, we used *MI*. That is, for a given recording, neural activity was measured at 90 probe locations, S_j ($j \in [1, 90]$). Neural activity *A*, either average power in different frequency bands or average firing rate, was discretized into 6 quantiles, Q_i ($i \in [1, 5]$), containing equal numbers of trials. Neural activity below Q_1 was classified as A_1, between Q_{i-1} and Q_i as A_i, and above Q_5 as A_6. The *MI* between neural activity and probe locations was then approximated by

$$MI(A,S) = \left(\sum_{i=1}^{6} \sum_{j=1}^{90} \frac{M_{ij}}{M} \log_2 \frac{M_{ij} M}{M_{i\cdot} M_{\cdot j}} \right) - \text{Bias}, \qquad \text{(Equation 4)}$$

where M_{ij} is the number of trials classified as A_i in the response to probe S_j . $M_{i\cdot}$ and $M_{\cdot j}$ are the sums of M_{ij} over *j* and *i*, respectively. *M* is the number of total trials. The Bias term is computed as

$$\text{Bias} = \frac{1}{2M \log 2} (U_{AS} - U_A - U_S + 1), \qquad \text{(Equation 5)}$$

where U_{AS} is the number of nonzero M_{ij} for all *i* and *j*, U_A is the number of nonzero $M_{\cdot j}$ for all *i*, and U_S is the number of nonzero $M_{i\cdot}$ for all *j* (Ito and Doya, 2009).

For each estimated *MI*, we performed nonparametric permutation tests (1,000 repetitions) to assess its significance. The resulting average *MI* obtained from the permutation procedure was subtracted from all reported *MI* values.

SUPPLEMENTAL INFORMATION

Supplemental Information includes Supplemental Experimental Procedures and seven figures and can be found with this article online at https://doi.org/10.1016/j.celrep.2018.01.078.

ACKNOWLEDGMENTS

This work was supported by NIH EY014924 (T.M.). We thank Nikos Logothetis for helpful comments on a previous version of the manuscript. We thank Eshan Govil for technical assistance.

AUTHOR CONTRIBUTIONS

Conceptualization, X.C., M.Z., and T.M.; Methodology, X.C., M.Z., and T.M.; Validation, X.C., M.Z., and T.M.; Formal Analysis, X.C.; Investigation, M.Z.; Resources, T.M.; Writing – Original Draft, X.C., M.Z., and T.M.; Writing – Review & Editing, X.C., M.Z., and T.M.; Visualization, X.C. and M.Z.; Supervision, M.Z. and T.M.; Funding Acquisition, T.M.

DECLARATION OF INTERESTS

The authors declare no competing interests.

Received: May 8, 2017
Revised: October 30, 2017
Accepted: January 25, 2018
Published: February 20, 2018

REFERENCES

Barbas, H., and Pandya, D.N. (1989). Architecture and intrinsic connections of the prefrontal cortex in the rhesus monkey. J. Comp. Neurol. *286*, 353–375.

Belitski, A., Gretton, A., Magri, C., Murayama, Y., Montemurro, M.A., Logothetis, N.K., and Panzeri, S. (2008). Low-frequency local field potentials and spikes in primary visual cortex convey independent visual information. J. Neurosci. *28*, 5696–5709.

Berens, P., Logothetis, N.K., and Tolias, A.S. (2011). Local field potentials, BOLD, and spiking activity: relationships and physiological mechanisms. In Visual Population Codes: Toward a Common Multivariate Framework for Cell Recording and Functional Imaging, N. Kriegeskorte and G. Kreiman, eds. (The MIT Press), pp. 599–623.

Bruce, C.J., Goldberg, M.E., Bushnell, M.C., and Stanton, G.B. (1985). Primate frontal eye fields. II. Physiological and anatomical correlates of electrically evoked eye movements. J. Neurophysiol. *54*, 714–734.

Buffalo, E.A., Fries, P., Landman, R., Buschman, T.J., and Desimone, R. (2011). Laminar differences in gamma and alpha coherence in the ventral stream. Proc. Natl. Acad. Sci. USA *108*, 11262–11267.

Burns, S.P., Xing, D., and Shapley, R.M. (2010). Comparisons of the dynamics of local field potential and multiunit activity signals in macaque visual cortex. J. Neurosci. *30*, 13739–13749.

Burr, D.C., Ross, J., Binda, P., and Morrone, M.C. (2010). Saccades compress space, time and number. Trends Cogn. Sci. *14*, 528–533.

Buschman, T.J., and Miller, E.K. (2009). Serial, covert shifts of attention during visual search are reflected by the frontal eye fields and correlated with population oscillations. Neuron *63*, 386–396.

Buzsáki, G., Anastassiou, C.A., and Koch, C. (2012). The origin of extracellular fields and currents–EEG, ECoG, LFP and spikes. Nat. Rev. Neurosci. *13*, 407–420.

Cardin, J.A., Carlén, M., Meletis, K., Knoblich, U., Zhang, F., Deisseroth, K., Tsai, L.H., and Moore, C.I. (2009). Driving fast-spiking cells induces gamma rhythm and controls sensory responses. Nature *459*, 663–667.

Chandrasekaran, C., Peixoto, D., Newsome, W.T., and Shenoy, K.V. (2017). Laminar differences in decision-related neural activity in dorsal premotor cortex. Nat. Commun. *8*, 614.

Chelazzi, L., Miller, E.K., Duncan, J., and Desimone, R. (1993). A neural basis for visual search in inferior temporal cortex. Nature *363*, 345–347.

Chen, C.M., Lakatos, P., Shah, A.S., Mehta, A.D., Givre, S.J., Javitt, D.C., and Schroeder, C.E. (2007). Functional anatomy and interaction of fast and slow visual pathways in macaque monkeys. Cereb. Cortex *17*, 1561–1569.

Chen, X., Scangos, K.W., and Stuphorn, V. (2010). Supplementary motor area exerts proactive and reactive control of arm movements. J. Neurosci. *30*, 14657–14675.

Connor, C.E., Gallant, J.L., Preddie, D.C., and Van Essen, D.C. (1996). Responses in area V4 depend on the spatial relationship between stimulus and attention. J. Neurophysiol. *75*, 1306–1308.

Desimone, R., Chelazzi, L., Miller, E., and Duncan, J. (1994). Neural Mechanisms for Memory-Guided Visual Search. Exp. Brain Res. *24*, 279–285.

Deubel, H., Schneider, W.X., and Bridgeman, B. (1996). Postsaccadic target blanking prevents saccadic suppression of image displacement. Vision Res. *36*, 985–996.

Duhamel, J.R., Colby, C.L., and Goldberg, M.E. (1992). The updating of the representation of visual space in parietal cortex by intended eye movements. Science *255*, 90–92.

Eckhorn, R., Bauer, R., Jordan, W., Brosch, M., Kruse, W., Munk, M., and Reitboeck, H.J. (1988). Coherent oscillations: a mechanism of feature linking in the visual cortex? Multiple electrode and correlation analyses in the cat. Biol. Cybern. *60*, 121–130.

Einevoll, G.T., Kayser, C., Logothetis, N.K., and Panzeri, S. (2013). Modelling and analysis of local field potentials for studying the function of cortical circuits. Nat. Rev. Neurosci. *14*, 770–785.

Engel, T.A., Steinmetz, N.A., Gieselmann, M.A., Thiele, A., Moore, T., and Boahen, K. (2016). Selective modulation of cortical state during spatial attention. Science *354*, 1140–1144.

Fischer, B., and Boch, R. (1981). Enhanced activation of neurons in prelunate cortex before visually guided saccades of trained rhesus monkeys. Exp. Brain Res. *44*, 129–137.

Frien, A., Eckhorn, R., Bauer, R., Woelbern, T., and Gabriel, A. (2000). Fast oscillations display sharper orientation tuning than slower components of the same recordings in striate cortex of the awake monkey. Eur. J. Neurosci. *12*, 1453–1465.

Fries, P., Reynolds, J.H., Rorie, A.E., and Desimone, R. (2001). Modulation of oscillatory neuronal synchronization by selective visual attention. Science *291*, 1560–1563.

Gabbott, P.L., and Bacon, S.J. (1996). Local circuit neurons in the medial prefrontal cortex (areas 24a,b,c, 25 and 32) in the monkey: II. Quantitative areal and laminar distributions. J. Comp. Neurol. *364*, 609–636.

Gail, A., Brinksmeyer, H.J., and Eckhorn, R. (2004). Perception-related modulations of local field potential power and coherence in primary visual cortex of awake monkey during binocular rivalry. Cereb. Cortex *14*, 300–313.

Gerbella, M., Belmalih, A., Borra, E., Rozzi, S., and Luppino, G. (2010). Cortical connections of the macaque caudal ventrolateral prefrontal areas 45A and 45B. Cereb. Cortex *20*, 141–168.

Gieselmann, M.A., and Thiele, A. (2008). Comparison of spatial integration and surround suppression characteristics in spiking activity and the local field potential in macaque V1. Eur. J. Neurosci. *28*, 447–459.

Godlove, D.C., Maier, A., Woodman, G.F., and Schall, J.D. (2014). Microcircuitry of agranular frontal cortex: testing the generality of the canonical cortical microcircuit. J. Neurosci. *34*, 5355–5369.

Gray, C.M., and Singer, W. (1989). Stimulus-specific neuronal oscillations in orientation columns of cat visual cortex. Proc. Natl. Acad. Sci. USA *86*, 1698–1702.

Gregoriou, G.G., Rossi, A.F., Ungerleider, L.G., and Desimone, R. (2014). Lesions of prefrontal cortex reduce attentional modulation of neuronal responses and synchrony in V4. Nat. Neurosci. *17*, 1003–1011.

Haider, B., Schulz, D.P.A., Häusser, M., and Carandini, M. (2016). Millisecond Coupling of Local Field Potentials to Synaptic Currents in the Awake Visual Cortex. Neuron *90*, 35–42.

Hamker, F.H., Zirnsak, M., Calow, D., and Lappe, M. (2008). The peri-saccadic perception of objects and space. PLoS Comput. Biol. *4*, e31.

Hartmann, T.S., Zirnsak, M., Marquis, M., Hamker, F.H., and Moore, T. (2017). Two Types of Receptive Field Dynamics in Area V4 at the Time of Eye Movements? Front. Syst. Neurosci. *11*, 13.

Henrie, J.A., and Shapley, R. (2005). LFP power spectra in V1 cortex: the graded effect of stimulus contrast. J. Neurophysiol. *94*, 479–490.

Huerta, M.F., Krubitzer, L.A., and Kaas, J.H. (1987). Frontal eye field as defined by intracortical microstimulation in squirrel monkeys, owl monkeys, and macaque monkeys. II. Cortical connections. J. Comp. Neurol. *265*, 332–361.

Hwang, E.J., and Andersen, R.A. (2012). Spiking and LFP activity in PRR during symbolically instructed reaches. J. Neurophysiol. *107*, 836–849.

Ito, M., and Doya, K. (2009). Validation of decision-making models and analysis of decision variables in the rat basal ganglia. J. Neurosci. *29*, 9861–9874.

Kaiser, M., and Lappe, M. (2004). Perisaccadic mislocalization orthogonal to saccade direction. Neuron *41*, 293–300.

Kastner, S., and Ungerleider, L.G. (2001). The neural basis of biased competition in human visual cortex. Neuropsychologia *39*, 1263–1276.

Katzner, S., Nauhaus, I., Benucci, A., Bonin, V., Ringach, D.L., and Carandini, M. (2009). Local origin of field potentials in visual cortex. Neuron *61*, 35–41.

Khawaja, F.A., Tsui, J.M., and Pack, C.C. (2009). Pattern motion selectivity of spiking outputs and local field potentials in macaque visual cortex. J. Neurosci. *29*, 13702–13709.

Liu, J., and Newsome, W.T. (2006). Local field potential in cortical area MT: stimulus tuning and behavioral correlations. J. Neurosci. *26*, 7779–7790.

Luck, S.J., Chelazzi, L., Hillyard, S.A., and Desimone, R. (1997). Neural mechanisms of spatial selective attention in areas V1, V2, and V4 of macaque visual cortex. J. Neurophysiol. *77*, 24–42.

McConkie, G.W., and Currie, C.B. (1996). Visual stability across saccades while viewing complex pictures. J. Exp. Psychol. Hum. Percept. Perform. *22*, 563–581.

Mejias, J.F., Murray, J.D., Kennedy, H., and Wang, X.J. (2016). Feedforward and feedback frequency-dependent interactions in a large-scale laminar network of the primate cortex. Sci. Adv. *2*, e1601335.

Merrikhi, Y., Clark, K., Albarran, E., Parsa, M., Zirnsak, M., Moore, T., and Noudoost, B. (2017). Spatial working memory alters the efficacy of input to visual cortex. Nat. Commun. *8*, 15041.

Mineault, P.J., Zanos, T.P., and Pack, C.C. (2013). Local field potentials reflect multiple spatial scales in V4. Front. Comput. Neurosci. *7*, 21.

Mitzdorf, U. (1985). Current source-density method and application in cat cerebral cortex: investigation of evoked potentials and EEG phenomena. Physiol. Rev. *65*, 37–100.

Moore, T., and Zirnsak, M. (2017). Neural Mechanisms of Selective Visual Attention. Annu. Rev. Psychol. *68*, 47–72.

Moore, T., Tolias, A.S., and Schiller, P.H. (1998). Visual representations during saccadic eye movements. Proc. Natl. Acad. Sci. USA *95*, 8981–8984.

Moran, J., and Desimone, R. (1985). Selective attention gates visual processing in the extrastriate cortex. Science *229*, 782–784.

Nandy, A.S., Nassi, J.J., and Reynolds, J.H. (2017). Laminar Organization of Attentional Modulation in Macaque Visual Area V4. Neuron *93*, 235–246.

Nicholson, C., and Freeman, J.A. (1975). Theory of current source-density analysis and determination of conductivity tensor for anuran cerebellum. J. Neurophysiol. *38*, 356–368.

Pesaran, B., Pezaris, J.S., Sahani, M., Mitra, P.P., and Andersen, R.A. (2002). Temporal structure in neuronal activity during working memory in macaque parietal cortex. Nat. Neurosci. *5*, 805–811.

Rasch, M.J., Gretton, A., Murayama, Y., Maass, W., and Logothetis, N.K. (2008). Inferring spike trains from local field potentials. J. Neurophysiol. *99*, 1461–1476.

Ray, S., and Maunsell, J.H. (2010). Differences in gamma frequencies across visual cortex restrict their possible use in computation. Neuron *67*, 885–896.

Ray, S., and Maunsell, J.H. (2011). Different origins of gamma rhythm and high-gamma activity in macaque visual cortex. PLoS Biol. *9*, e1000610.

Ray, S., Hsiao, S.S., Crone, N.E., Franaszczuk, P.J., and Niebur, E. (2008). Effect of stimulus intensity on the spike-local field potential relationship in the secondary somatosensory cortex. J. Neurosci. *28*, 7334–7343.

Reynolds, J.H., and Chelazzi, L. (2004). Attentional modulation of visual processing. Annu. Rev. Neurosci. *27*, 611–647.

Reynolds, J.H., Chelazzi, L., and Desimone, R. (1999). Competitive mechanisms subserve attention in macaque areas V2 and V4. J. Neurosci. *19*, 1736–1753.

Ross, J., Morrone, M.C., and Burr, D.C. (1997). Compression of visual space before saccades. Nature *386*, 598–601.

Saalmann, Y.B., Pinsk, M.A., Wang, L., Li, X., and Kastner, S. (2012). The pulvinar regulates information transmission between cortical areas based on attention demands. Science *337*, 753–756.

Schall, J.D., Morel, A., King, D.J., and Bullier, J. (1995). Topography of visual cortex connections with frontal eye field in macaque: convergence and segregation of processing streams. J. Neurosci. *15*, 4464–4487.

Schmolesky, M.T., Wang, Y., Hanes, D.P., Thompson, K.G., Leutgeb, S., Schall, J.D., and Leventhal, A.G. (1998). Signal timing across the macaque visual system. J. Neurophysiol. *79*, 3272–3278.

Schroeder, C.E., Mehta, A.D., and Givre, S.J. (1998). A spatiotemporal profile of visual system activation revealed by current source density analysis in the awake macaque. Cereb. Cortex *8*, 575–592.

Self, M.W., Peters, J.C., Possel, J.K., Reithler, J., Goebel, R., Ris, P., Jeurissen, D., Reddy, L., Claus, S., Baayen, J.C., and Roelfsema, P.R. (2016). The

Effects of Context and Attention on Spiking Activity in Human Early Visual Cortex. PLoS Biol. *14*, e1002420.

Sheinberg, D.L., and Logothetis, N.K. (2001). Noticing familiar objects in real world scenes: the role of temporal cortical neurons in natural vision. J. Neurosci. *21*, 1340–1350.

Siegle, J.H., Pritchett, D.L., and Moore, C.I. (2014). Gamma-range synchronization of fast-spiking interneurons can enhance detection of tactile stimuli. Nat. Neurosci. *17*, 1371–1379.

Silva, L.R., Amitai, Y., and Connors, B.W. (1991). Intrinsic oscillations of neocortex generated by layer 5 pyramidal neurons. Science *251*, 432–435.

Sommer, M.A., and Wurtz, R.H. (2004). What the brain stem tells the frontal cortex. I. Oculomotor signals sent from superior colliculus to frontal eye field via mediodorsal thalamus. J. Neurophysiol. *91*, 1381–1402.

Sommer, M.A., and Wurtz, R.H. (2006). Influence of the thalamus on spatial visual processing in frontal cortex. Nature *444*, 374–377.

Stanton, G.B., Bruce, C.J., and Goldberg, M.E. (1995). Topography of projections to posterior cortical areas from the macaque frontal eye fields. J. Comp. Neurol. *353*, 291–305.

Tolias, A.S., Moore, T., Smirnakis, S.M., Tehovnik, E.J., Siapas, A.G., and Schiller, P.H. (2001). Eye movements modulate visual receptive fields of V4 neurons. Neuron *29*, 757–767.

Tremblay, S., Doucet, G., Pieper, F., Sachs, A., and Martinez-Trujillo, J. (2015). Single-Trial Decoding of Visual Attention from Local Field Potentials in the Primate Lateral Prefrontal Cortex Is Frequency-Dependent. J. Neurosci. *35*, 9038–9049.

Tremblay, R., Lee, S., and Rudy, B. (2016). GABAergic Interneurons in the Neocortex: From Cellular Properties to Circuits. Neuron *91*, 260–292.

Ungerleider, L.G., and Desimone, R. (1986). Cortical connections of visual area MT in the macaque. J. Comp. Neurol. *248*, 190–222.

van Kerkoerle, T., Self, M.W., Dagnino, B., Gariel-Mathis, M.A., Poort, J., van der Togt, C., and Roelfsema, P.R. (2014). Alpha and gamma oscillations characterize feedback and feedforward processing in monkey visual cortex. Proc. Natl. Acad. Sci. USA *111*, 14332–14341.

Vijayan, S., and Kopell, N.J. (2012). Thalamic model of awake alpha oscillations and implications for stimulus processing. Proc. Natl. Acad. Sci. USA *109*, 18553–18558.

Wang, X., Fung, C.C., Guan, S., Wu, S., Goldberg, M.E., and Zhang, M. (2016). Perisaccadic Receptive Field Expansion in the Lateral Intraparietal Area. Neuron *90*, 400–409.

Wilke, M., Logothetis, N.K., and Leopold, D.A. (2006). Local field potential reflects perceptual suppression in monkey visual cortex. Proc. Natl. Acad. Sci. USA *103*, 17507–17512.

Wimmer, K., Ramon, M., Pasternak, T., and Compte, A. (2016). Transitions between Multiband Oscillatory Patterns Characterize Memory-Guided Perceptual Decisions in Prefrontal Circuits. J. Neurosci. *36*, 489–505.

Womelsdorf, T., Fries, P., Mitra, P.P., and Desimone, R. (2006). Gamma-band synchronization in visual cortex predicts speed of change detection. Nature *439*, 733–736.

Wurtz, R.H. (2008). Neuronal mechanisms of visual stability. Vision Res. *48*, 2070–2089.

Xu, X., Roby, K.D., and Callaway, E.M. (2010). Immunochemical characterization of inhibitory mouse cortical neurons: three chemically distinct classes of inhibitory cells. J. Comp. Neurol. *518*, 389–404.

Zhao, M., Gersch, T.M., Schnitzer, B.S., Dosher, B.A., and Kowler, E. (2012). Eye movements and attention: the role of pre-saccadic shifts of attention in perception, memory and the control of saccades. Vision Res. *74*, 40–60.

Zirnsak, M., and Moore, T. (2014). Saccades and shifting receptive fields: anticipating consequences or selecting targets? Trends Cogn. Sci. *18*, 621–628.

Zirnsak, M., Steinmetz, N.A., Noudoost, B., Xu, K.Z., and Moore, T. (2014). Visual space is compressed in prefrontal cortex before eye movements. Nature *507*, 504–507.

Cell Reports, Volume *22*

Supplemental Information

Dissonant Representations of Visual Space in Prefrontal Cortex during Eye Movements

Xiaomo Chen, Marc Zirnsak, and Tirin Moore

General Surgical and Electrophysiological Procedures

Each animal was surgically implanted with a titanium head post, a scleral search coil, and a cylindrical titanium recording chamber (20 mm diameter) overlaying the arcuate sulcus. A craniotomy was performed on each animal, allowing access to the FEF. All surgeries were conducted using aseptic techniques under general anaesthesia (isoflurane), and analgesics were provided during post-surgical recovery.

Electrodes were lowered into the cortex using a hydraulic microdrive (Narishige International). Activity was recorded extracellularly using linear array electrodes (U-Probe, Plexon) with 16 contacts spaced 150 mm apart. Neural activity was measured against a local reference (e.g., Britten et al., 1993; Hikosaka and Watanabe, 2000), a stainless steel guide tube, which carried the electrode array and which was positioned above the dura. At the preamplifier stage, signals were processed with 0.5 Hz 1-pole high-pass and 8kHz 4-pole low-pass anti-aliasing Bessel filters, and then divided into two streams for the recording of LFPs and spiking activity. The stream used for LFP recording was amplified (×500~2000 gain), processed by a 4-pole 200Hz low-pass Bessel filter and sampled at 1000 Hz. The stream used for spike detection was processed by a 4-pole Bessel high-pass filter (300 Hz) a 2-pole Bessel low-passed filter (6000 Hz), and was sampled at 40 kHz. No other filters were used in the analyses.

The FEF was identified by the ability to evoke fixed-vector, short-latency saccadic eye movements with stimulation at low currents (Bruce and Goldberg, 1985; Moore and Fallah, 2001). U-Probes were then lowered for simultaneous measurements of visual LFP and spiking activity derived RFs at the same coordinates. After reaching the target depth we let the electrode settle for at least an hour before starting the recordings.

RF Measurements and Monkey Behavior

The visual probes to measure RFs consisted of white squares with an area of 1 dva^2 resulting in a positive luminance contrast of 60% (Michelson) and 3 (Weber) to the grey background (23.7 cd m^{-2}). The probe duration was less than 25 ms as measured with a photodiode.

In all three experimental conditions (Fixation 1, Fixation 2 and Presaccadic) the monkey was required to fixate one out of two fixation points (FP1 and FP2) placed 12 dva apart along the horizontal meridian. The fixation points FP1 and FP2 consisted of small (0.5 dva in diameter) red dots (23.6 cd m^{-2}). The saccade task consisted of a standard step task (Sommer and Wurtz, 2006) in which the fixation point (FP1) was displaced to a new location (FP2) and the monkey was rewarded for shifting its gaze to it. The fixation and presaccadic conditions differed in terms of the timing of the visual probe stimulus with respect to the saccade. In the two fixation conditions, the probe stimulus was presented at least 500 ms before a saccade. In the presaccadic condition, the probe presentation occurred while the monkey was still fixating at the location of FP1 but already planning a saccade to FP2. The monkey was rewarded with a drop of juice if he was still fixating at the required location at the end of the trial (>500 ms after probe presentation).

Fixation and saccade accuracy was excellent in both monkeys, with an average horizontal error of 0.01 dva (s.d. = 0.29) and an average vertical error of -0.02 dva (s.d. = 0.29) in fixation. The average saccade vector was 11.98 dva (s.d. = 0.52) with a horizontal landing error of -0.19 (s.d. = 0.35) and a vertical error of -0.05 dva (s.d. = 0.4). The average saccadic reaction time, that is, the time between target onset and saccade initiation, for monkey B was 229 ms (s.d. = 37) and 113 ms (s.d. = 35) for monkey N. For all reported analyses we used the responses to probes that were presented within a time window of 150 ms before saccade onset. Trials in which the probe was still on the screen when the saccade started, or was presented after the saccade, were excluded from the analyses. The average probe onset time was 82 ms before saccade onset (s.d. 38) for monkey B and 64 ms (s.d. 32) for monkey N; for further details see Zirnsak et al. (2014).

Power Spectral Density

Power spectral densities (PSDs) were calculated using Thomsons's multitaper method (e.g., Gregoriou et al., 2009; Jarvis and Mitra, 2001; Pesaran et al., 2008). Four orthogonal discrete prolate spheroidal (Slepian) sequences were used in the analysis. The frequency resolution of this method depends on the length of the signal. For example, for a 250 ms long LFP response, the frequency resolution is 4 Hz. On each trial, the baseline PSD was estimated using the LFPs during the period from (-350, -100] ms before probe onset. The baseline PSD was then subtracted from the stimulus or event related PSD. During fixation, we examined the periods from (0, 250] ms after probe onset. During the presaccadic period, we examined the time intervals from (0, 250] ms after probe onset, and (0, 250] ms, (125, 375] ms, (250, 500] ms, and (0, 500] ms after saccade onset.

Perpendicular Recordings and Current Source Density Analysis

We classified each linear array recording as either perpendicular or tangential based on the amount of RF displacement across array channels. Both LFP derived and spiking-derived RFs were used in the overall measure of the displacement. The displacement was measured as the systematic change in RF centers across channels and was computed via regression analyses on the RF centers. Recordings yielding significant regression coefficients were classified as tangential and recordings yielding non-significant

coefficients were classified as perpendicular (Figure 3A).

For the perpendicular recordings, we used current source density (CSD) analyses (Pettersen et al., 2006) to identify superficial, "granular", and deep layers of the FEF. The average LFP response during fixation across all probe locations was used for these analyses. Using only the RF center probe location yielded similar results, but was less reliable given the smaller number of trials. The CSD was calculated as the discrete double spatial derivative (Nicholson and Freeman, 1975) with "Vaknin" electrodes to yield the same number of CSD 'channels' as electrode channels (Vaknin et al., 1988). The CSD pattern was consistent across the 9 perpendicular penetrations and differed markedly from the tangential ones (Figure 3C). Within the perpendicular CSD pattern, the input ("granular") layer was defined as the compartment with a robust sink, which lay at a depth approximately corresponding to layer 4 of the FEF (0.7 – 1.0 mm). Superficial and deep layers, which had clearly different CSD, were defined as the compartments above and below the "granular layer".

REFERENCES

Britten, K.H., Shadlen, M.N., Newsome, W.T., and Movshon, J.A. (1993). Responses of neurons in macaque MT to stochastic motion signals. Vis Neurosci *10*, 1157-1169.

Bruce, C.J., and Goldberg, M.E. (1985). Primate frontal eye fields. I. Single neurons discharging before saccades. J Neurophysiol *53*, 603-635.

Gregoriou, G.G., Gotts, S.J., Zhou, H., and Desimone, R. (2009). High-frequency, long-range coupling between prefrontal and visual cortex during attention. Science *324*, 1207-1210.

Hikosaka, K., and Watanabe, M. (2000). Delay activity of orbital and lateral prefrontal neurons of the monkey varying with different rewards. Cereb Cortex *10*, 263-271.

Jarvis, M.R., and Mitra, P.P. (2001). Sampling properties of the spectrum and coherency of sequences of action potentials. Neural computation *13*, 717-749.

Moore, T., and Fallah, M. (2001). Control of eye movements and spatial attention. Proc Natl Acad Sci U S A *98*, 1273-1276.

Pesaran, B., Nelson, M.J., and Andersen, R.A. (2008). Free choice activates a decision circuit between frontal and parietal cortex. Nature *453*, 406-409.

Pettersen, K.H., Devor, A., Ulbert, I., Dale, A.M., and Einevoll, G.T. (2006). Current-source density estimation based on inversion of electrostatic forward solution: effects of finite extent of neuronal activity and conductivity discontinuities. J Neurosci Methods *154*, 116-133.

Vaknin, G., Discenna, P.G., and Teyler, T.J. (1988). A Method for Calculating Current Source Density (Csd) Analysis without Resorting to Recording Sites Outside the Sampling Volume. J Neurosci Meth *24*, 131-135.

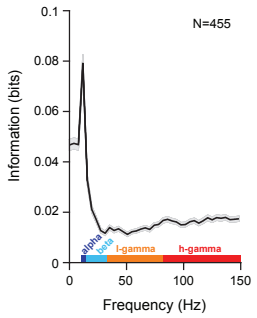

Figure S1. Mutual Information about Stimulus Location across LFP Frequencies, Related to Figure 1.

Mutual information was computed in discrete non-overlapping steps at 4 Hz resolutions. LFP frequency bands (alpha, beta, low-gamma, high-gamma) used for analyses are shown color-coded on top of the x-axis.

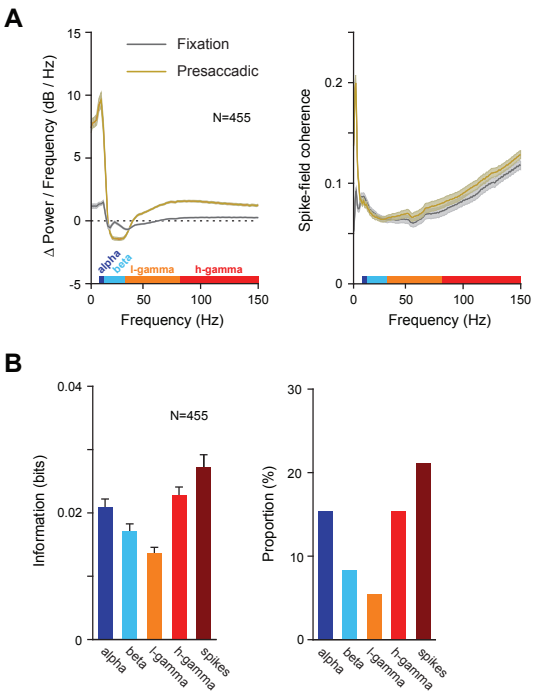

Figure S2. LFP Derived Visual Signals during Fixation and at the Time of Eye Movements, Related to Figure 1 & 5.

(A) Comparison of LFP power spectra and spike-field coherence. The left graph shows the LFP power spectra during fixation (gray) and at the time of saccades (gold). The shaded areas denote the standard error of the mean. The right graph shows the spike-field coherence during fixation (gray) and at the time of saccades (gold). Target LFP frequency bands used for analyses reported in the main text are shown color-coded on top of the x-axis of both graphs.

(B) Comparison of visual spatial information across different frequency bands. The left graph shows the average amount of mutual information about visual probe location contained within the LFP responses for a given frequency band and contained within the spiking activity, for the Presaccadic condition. Error bars denote the standard error of the mean. The right graph shows the percentage of recording sites across all experimental sessions, which yielded statistically significant mutual information for the different LFP frequency bands and the spiking activity. Although the LFP power and the spike-field coherence was generally higher during eye movement preparation for most frequencies as compared to fixation, the overall mutual information about the stimulus location and the number of recording sites yielding significant mutual information was lower.

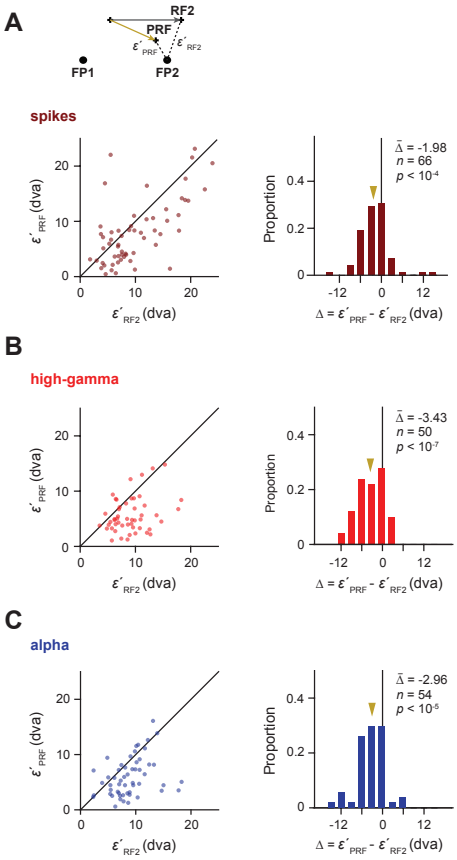

Figure S3. Comparison of Distances of the PRF and RF2 to FP2 ($\varepsilon'_{\mathrm{PRF}}$ $vs.$ $\varepsilon'_{\mathrm{RF2}}$) for all Significant Presaccadic RFs, Related to Figure 5.

(A) The graph shows $\varepsilon'_{\mathrm{PRF}}$ plotted against $\varepsilon'_{\mathrm{RF2}}$ for spiking RFs. PRFs were estimated from saccade aligned responses ((0-500] ms). The black line in the scatter plot denotes the line of unity. The gold vector in the histogram indicates the mean of the distribution.

(B) Comparison of $\varepsilon'_{\mathrm{PRF}}$ and $\varepsilon'_{\mathrm{RF2}}$ for high-gamma-band-derived RFs. Same conventions as in A.

(C) Comparison of $\varepsilon'_{\mathrm{PRF}}$ and $\varepsilon'_{\mathrm{RF2}}$ for alpha-band-derived RFs. Same conventions as in A. For all shown comparisons, PRFs are significantly closer to the saccade target than the RF2s.

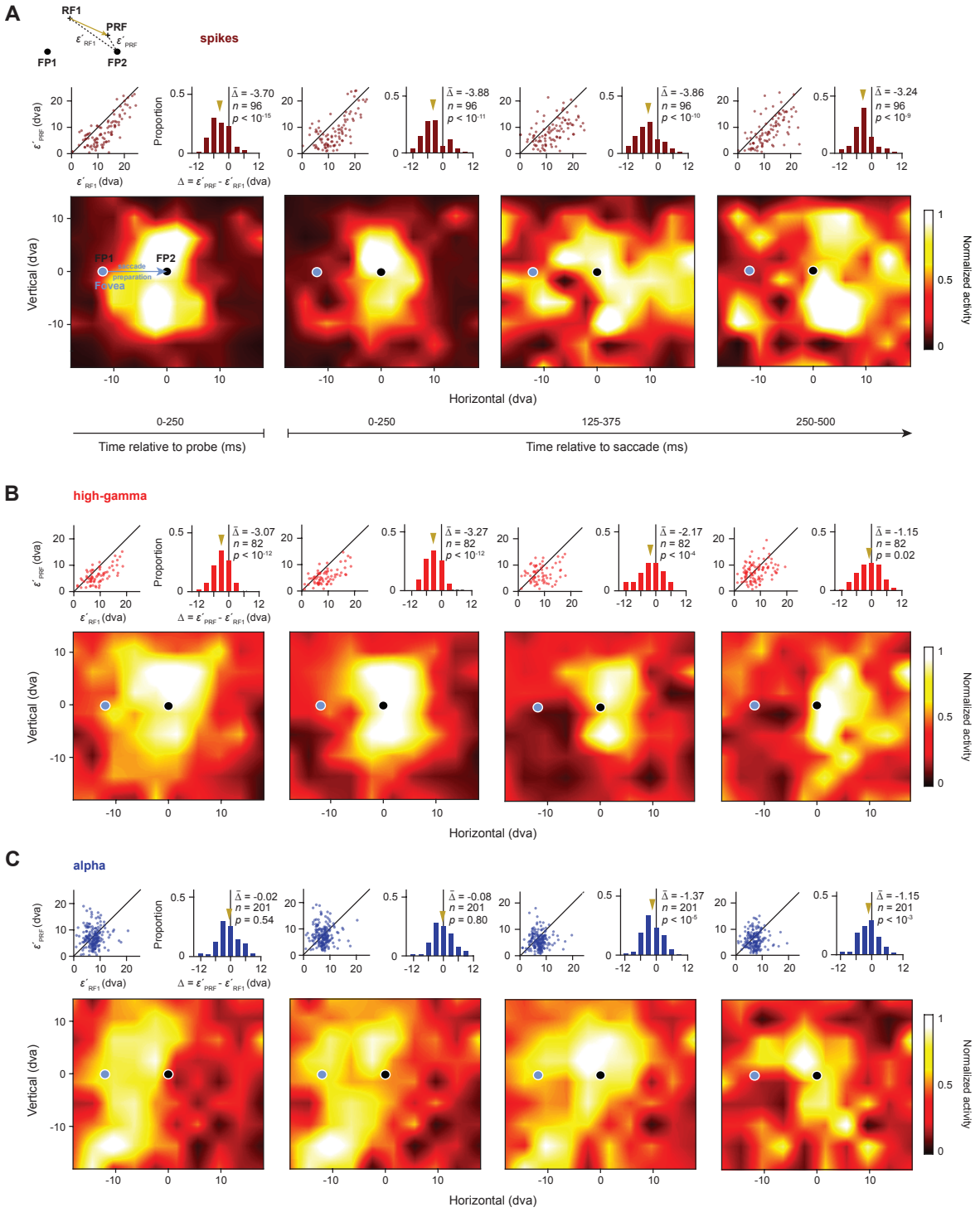

Figure S4. Dissociation of Alpha and High-gamma RFs at the Time of Eye Movements for all Significant Fixation RFs, Related to Figure 5.

(A) Population RFs derived from spiking activity to probes presented during saccade preparation from fixation point 1 (FP1) to fixation point 2 (FP2). Each map shows the population RF based on responses at different times relative to the eye movement. From left to right, Population RF aligned to probe onset (0-250] ms, Population RFs aligned to saccade onset (0-250] ms, (125-375] ms, and (250-500] ms. Bright areas indicate high levels of activity whereas dark areas depict low levels of activity. The insets on top of each population RF compare the distance $\varepsilon'_{\mathrm{PRF}}$ between the presaccadic RF centers (PRFs) and the saccade target (FP2) to the distance $\varepsilon'_{\mathrm{RF1}}$ between the fixation 1 RF centers (RF1s) and the FP2 for all significant fixation RFs (fixation 1 and fixation 2) (see Supplemental Experimental Procedures). Solid lines in the scatter plots depict the line of unity. Gold arrows in the histograms indicate the mean of the population.

(B) Population RFs derived from the high-gamma band. Same conversions as in A.

(C) Population RFs derived from the alpha band. Same conversions as in A. The population RFs have been spatially interpolated for visualization. In Figure 4, all population RFs and RF centers are based on, respectively from, statistically significant individual presaccadic RFs. Here we show the same results for recording sites with significant RFs during both Fixation 1 and Fixation 2 irrespective of their significance during the presaccadic epoch.

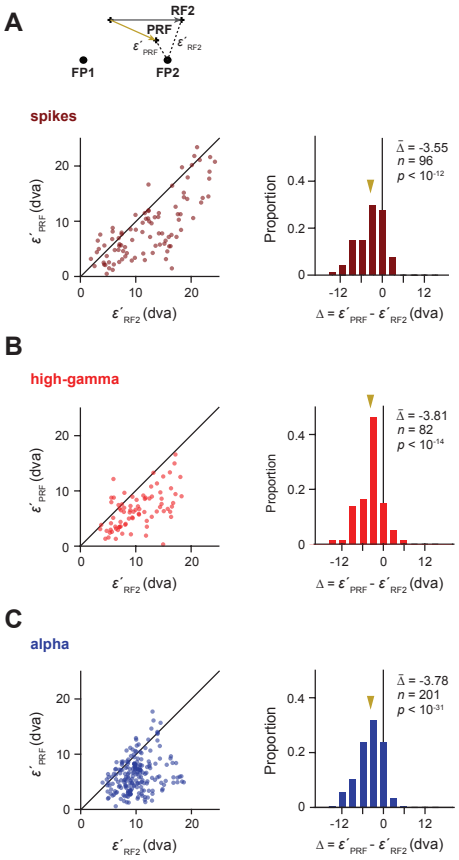

Figure S5. PRF to RF2 Comparison for all Significant Fxation RFs, Related to Figure 5.

(A) The graph shows $\varepsilon'_{\mathrm{PRF}}$ (distance between the PRF and FP2) plotted against $\varepsilon'_{\mathrm{RF2}}$ (distance between the RF2 and FP2) for spiking RFs. PRFs were estimated from saccade aligned responses ((0-500] ms). The black line in the scatter plot denotes the line of unity. The gold vector in the histogram indicates the mean of the distribution.

(B) Comparison of $\varepsilon'_{\mathrm{PRF}}$ and $\varepsilon'_{\mathrm{RF2}}$ for high-gamma-band-derived RFs. Same conventions as in A.

(C) Comparison of $\varepsilon'_{\mathrm{PRF}}$ and $\varepsilon'_{\mathrm{RF2}}$ for alpha-band-derived RFs. Same conventions as in A. For all shown comparisons, PRFs are significantly closer to the saccade target than the RF2s.

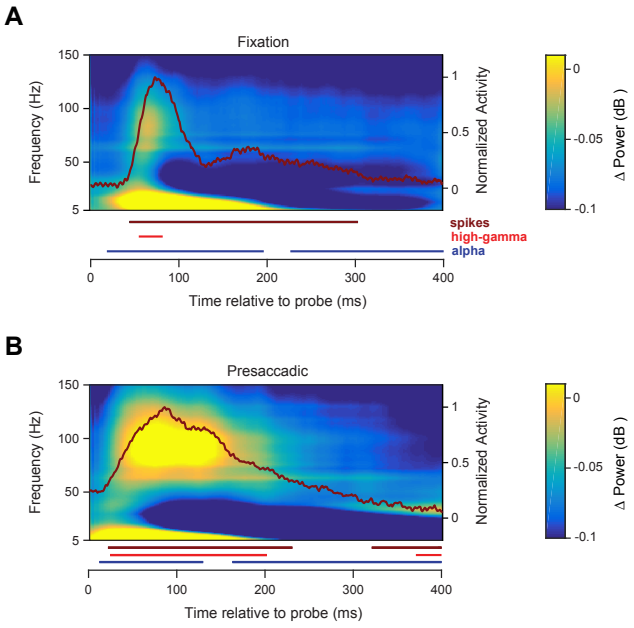

Figure S6. Average Time-frequency Power Spectra and Simultaneously Recorded Spiking Activities, Related to Figure 6.
(A) Average time-frequency spectrum and spiking activity across recordings and all stimulus locations relative to probe onset for the fixation conditions. Matching pursuit decomposition was used in calculating the spectrum to optimize temporal and frequency resolutions. An exponential kernel was used to estimate the average firing rate. Each spike therefore influences the estimate only forward in time. Lines below the graph indicate significant differences from baseline for the alpha band (blue), the high-gamma band (red), and the spiking activity (dark red).
(B) Average time-frequency spectrum and spiking activity relative across recordings and all stimulus locations to probe onset for the presaccadic condition. All the time-frequency spectra have been interpolated in both the frequency and temporal domain for visualization.

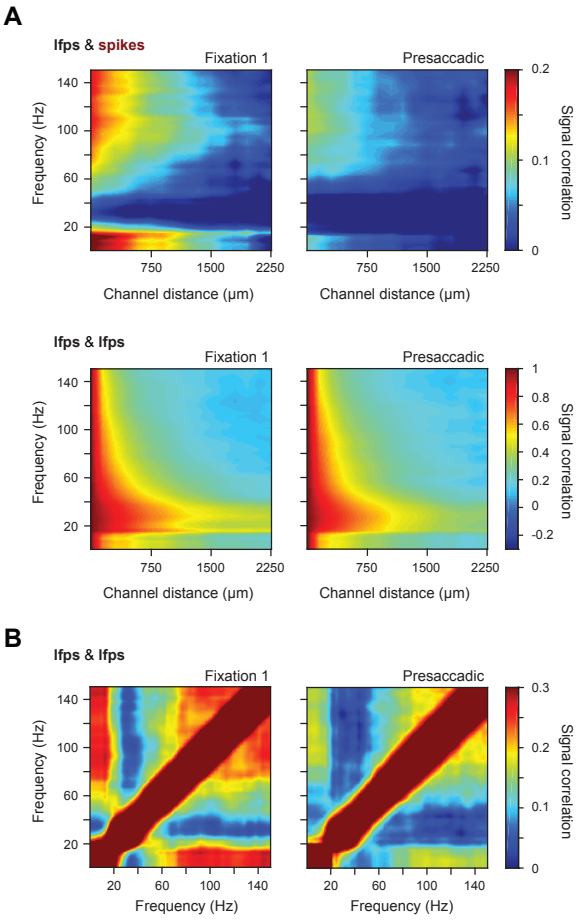

Figure S7. Comparison of Signal Correlations during Fixation and at the Time of Eye Movements, Related to Figure 6.

(A) Top, signal correlations between spiking responses to visual probes recorded at a reference channel (0 μm) and LFP responses recorded at distant channels of the linear electrode probe. Bottom, signal correlations between LFP responses recorded at a reference channel (0 μm) and LFP responses recorded at distant channels. The results has been spatially interpolated for visualization.

(B) Average signal correlation between different LFP frequencies recorded at the same electrode channels across all experimental sessions. Left, Fixation 1; right, Presaccadic. The results have been spatially interpolated for visualization